Assessing Marine Snow Dynamics During the Demise of the North Atlantic Spring Bloom Using In Situ Particle Imagery

Draft: May 17, 2025

Authors: D.A. Siegel[1,*], A.B. Burd[2], M.L. Estapa[3], E. Fields[1], L. Johnson[4], U. Passow[5], E. Romanelli[1,6], M.A. Brzezinski[7], K.O. Buesseler[8], S.J. Clevenger[9], I. Cetinić[10], L. Drago[11], C.A. Durkin[12], R. Kiko[13], S.J. Kramer[12], A.E. Maas[14], M.M. Omand[16] and D.K. Steinberg[16]

1 - Earth Research Institute and Department of Geography, University of California, Santa Barbara, Santa Barbara, CA, USA, david.siegel@ucsb.edu & fields@ucsb.edu
2 - Department of Marine Sciences, University of Georgia, Athens, GA, USA, adrianb@uga.edu
3 - School of Marine Sciences, Darling Marine Center, University of Maine, Walpole, ME, USA, margaret.estapa@maine.edu
4 - Applied Physics Laboratory, University of Washington, Seattle, WA, leahjohn@uw.edu
5 - Ocean Sciences Centre, Memorial University Newfoundland, St. John's, NL, Canada, uta.passow@mun.ca
6 - Institute of Environmental Engineering, Department of Civil, Environmental and Geomatic Engineering, ETH Zurich, Zurich, Switzerland, eromanelli@ethz.ch
7 - Marine Science Institute, University of California, Santa Barbara, Santa Barbara, CA, USA, markbrzezinski@lifesci.ucsb.edu
8 - Department of Marine Chemistry & Geochemistry, Woods Hole Oceanographic Institution, Woods Hole, MA 02543, USA, kbuesseler@whoi.edu
9 - MIT-WHOI Joint Program in Oceanography, Applied Ocean Science and Engineering, Cambridge, MA, USA, s.jade.clevenger@gmail.com
10 - GESTAR II, Morgan State University, Baltimore, MD, USA and Ocean Ecology Laboratory, NASA Goddard Space Flight Center, Greenbelt, MD, USA, ivona.cetinic@nasa.gov
11 - Laboratoire d'Océanographie de Villefranche, Sorbonne Université, Paris, France and Sorbonne Université, UMR 7159 CNRS-IRD-MNHN, LOCEAN-IPSL, Paris, France, laetitia.drago@locean.ipsl.fr
12 - Monterey Bay Aquarium Research Institute, Moss Landing, CA, USA, cdurkin@mbari.org & skramer@mbari.org
13 - Laboratoire d'Océanographie de Villefranche, Sorbonne Université, Paris, France & GEOMAR Helmholtz Centre for Ocean Research, Kiel, Germany, rkiko@geomar.de
14 - Bermuda Institute of Ocean Sciences, School of Ocean Futures, Arizona State University, St. George's, Bermuda, amaas4@asu.edu
15 - Graduate School of Oceanography, University of Rhode Island, Narragansett, RI, USA, momand@uri.edu
16 - Coastal and Ocean Processes Section, Virginia Institute of Marine Science, William & Mary, Gloucester Point, VA, USA, debbies@vims.edu

*corresponding author

Abstract:

The ocean's biological pump, a critical component of the Earth's carbon cycle, transports organic matter from the surface ocean to depth and is dominated by sinking particles, often in the form of marine snow-sized (diameter ≥ 0.5 mm) aggregates. Controls on sinking particle carbon export are thought to be driven largely by ecological processes that create and transform sinking particles. We diagnose the importance of both biotic and abiotic processes in the dynamics of marine snow using image-based determination of their size distribution. These observations were made during the demise of the North Atlantic spring bloom as part of the Export Processes in the Ocean from RemoTe Sensing North Atlantic (EXPORTS-NA) field campaign. We show that a sequence of intense storm events generated high turbulent mixing rates in the upper ocean that impacted the abundance, size distribution, porosity and sinking of marine snow aggregates. Mixed-layer turbulence both created and destroyed marine snow aggregates and the sequence of entrainment and detrainment of the mixed layer induced by repeated storm forcings enhanced the vertical transport of aggregates to depth. Evidence of biological transformations was also observed at mesopelagic depths, both for the consumption of aggregates and in the creation of small particles from larger ones, likely due to interactions with zooplankton. Collectively, these results illustrate the complex interplay of physical and biological processes regulating the dynamics of marine snow and suggest their inclusion in predictive models of the ocean's biological pump.

Plain Language Summary

The ocean's biological pump is a critical component of the Earth's carbon cycle, transporting roughly 10 Gigatons of organic carbon from the ocean's surface layers to its interior where it is sequestered from the atmosphere for months to millennia. The dominant pathway for the biological pump is via the sinking of organic particles and marine snow aggregates, which are amalgamations of largely detrital materials that are larger than one-half of a millimeter in diameter. Here, we address the dynamics of marine snow aggregates using in situ imagery observations of their size distribution during the demise of the North Atlantic spring bloom. We show the important roles that turbulence in the ocean surface layer has on the creation and destruction of marine snow aggregates and their transport to depth. We also quantify the interactions of sinking marine snow below the ocean surface layer with zooplankton; both consuming sinking organic matter, but also creating smaller particles from marine snow. Our results demonstrate the interplay of physical and biological processes controlling the dynamics of marine snow aggregates.

Short Title: On the Ephemeral Nature of Marine Snow

Key Points:

1. The characteristics of marine snow aggregates in the mixed layer are ephemeral, responding rapidly to large changes in turbulence due to the passage of storms.
2. The sequential passage of storms preconditioned aggregates characteristics leading to a large sinking plume of unusually large marine snow aggregates.
3. Biological processing in the mesopelagic zone is also seen likely due to the consumption of sinking marine snow and production of smaller particles by zooplankton.

Keywords: Marine Snow, Particle Aggregation and Disaggregation, Ocean Turbulence, Zooplankton, Spring Bloom Dynamics

1.0 Introduction

The ocean's biological pump transports organic matter, created by phytoplankton productivity in the well-lit surface ocean, to the ocean's dark interior, where it is consumed by animals and heterotrophic microbes and primarily remineralized back to inorganic forms (Ducklow et al. 2001; LeMoigne, 2019; Iversen, 2023; Burd, 2024). This downward transport of organic matter, dominated by the gravitational settling of particles including marine snow aggregates, sequesters respired carbon dioxide within the ocean on timescales of months to millennia, depending on the remineralization depth profile, ocean circulation and mixing (Siegel et al. 2023a; Nowicki et al. 2024). A predictive understanding of the biological pump's function is critical to assess its role in future climate states and to measure the efficacy and impacts of carbon dioxide removal interventions aimed at contributing to net negative greenhouse gas emissions (Henson et al. 2022; Doney et al. 2025).

Much of what has been learned about the ocean's biological pump has come from field studies where the life cycle of particles is followed from their production in the upper ocean to their export to depth (Ducklow et al. 2001; Siegel et al. 2016; Buesseler et al. 2020). Typical particle sinking speeds (roughly 10 to 100 m d^{-1}) dictate a 5-to-10-day timescale to study the upper 500 m of the water column. Metrics for the efficiency of the biological pump, such as the e-ratio (the export flux leaving the upper ocean divided by the net primary production, NPP), integrate biogeochemical fluxes over this time scale. The challenge arises when the biotic and abiotic factors driving NPP and particle export vary on shorter and/or differing time scales, such as during bloom events, or if there is lateral transport of sinking materials that would decouple near-surface observations of NPP from sinking particle export measurements made at depth, which could happen if the observations were not Lagrangian (Briggs et al. 2011; Henson et al. 2015; Siegel et al. 2016; Giering et al. 2017).

Characterization of the nature and dynamics of sinking particles is critical for understanding the links between NPP and sinking particle fluxes (LeMoigne, 2019; Iversen, 2023; Burd, 2024). Typical sizes of sinking particles are a few tens of microns to many millimeters (McDonnell and Buesseler, 2010; Durkin et al. 2021). These particles are larger than nearly all open ocean phytoplankton taxa, which range from 0.5 to ~50 μm (Marañón, 2015). Thus, the production of particulate materials via phytoplankton NPP in the euphotic zone needs to be transformed into sinking particles that are large enough to contribute to sinking particle fluxes. Of particular interest are marine snow aggregates, which rapidly sink through the water column as typical sinking speeds are many 10's to several 100 meters per day (Alldredge and Gotschalk, 1988). Marine snow is defined as particulate aggregates with equivalent spherical diameters greater than 0.5 mm (Alldredge and Silver, 1988), which are roughly 10 to 1,000 times larger than typical open ocean phytoplankton cells (Marañón, 2015).

Many biologically-mediated processes transform phytoplankton and suspended particles to sinking ones and back again to suspended particles. For example, zooplankton consume smaller particles and create larger particles through their production of fecal matter, feeding webs and their own carcasses (Steinberg and Landry, 2017; Iversen, 2023; Steinberg et al. 2023). Zooplankton also act to transform larger particles and aggregates back to small ones through fragmentation due to sloppy feeding and/or turbulent shears created by their swimming (Dilling et al. 1998; Dilling and Alldredge, 2000; Goldthwait et al. 2004). Fragmentation of particles will in turn enhance the solubilization of particles into dissolved forms which are widely available to the microbial community (Møller et al. 2003; Collins et al. 2015). Particle-associated microbial communities also consume and solubilize particulate matter on sinking particles (Collins et al. 2015; Belcher et al. 2016; Cram et al. 2018; Stephens et al. 2024). The balance among these many biotic processes controls the vertical attenuation of sinking particle fluxes as well as the supply of photosynthetically fixed energy to the deep sea (Steinberg et al. 2008; Buesseler and Boyd, 2009; Burd et al. 2010).

Abiotic processes can also transform particles and aggregates by promoting collisions that aggregate smaller particles into larger ones and disaggregate large particles into smaller ones by turbulent shear forces (Alldredge et al. 1990; Burd and Jackson, 1997). Coagulation between two particles can occur due to particle-particle encounters driven by turbulent shears or through differential sedimentation, where a faster sinking particle catches up and coagulates with a slower sinking one (Jackson, 1990). The formation rate of large aggregates will depend on the particle encounter rate and the abundances of source particles. Turbulent shears can also disaggregate large particles into smaller ones when the size of a marine snow aggregate becomes as large as the size of the smallest eddy in the flow, the Kolmogorov scale (Alldredge et al. 1990; Takeuchi et al. 2019; Song et al. 2024).

The net result of this amalgamation of transformative processes creating and destroying particulate aggregates is that individual marine snow aggregates are highly porous (Alldredge and Gotschalk, 1988; Laurenceau-Cornec et al. 2019). Typically, the solid fraction of a particle's volume, measured by its equivalent spherical diameter, ranges from 10^{-2} to 10^{-6}. The porous nature of marine aggregates will greatly affect the relationship between their volume and mass, requiring assessment of their fractal nature in any quantitative analysis (Logan and Alldredge 1989; Jackson, 1990; Stemmann et al., 2004; see Supplementary Section S7). The fractal nature of marine aggregates will also impact their sinking speed (Laurenceau-Cornec et al. 2019; Cael et al. 2021).

Here, we examine field observations of the demise of the North Atlantic spring bloom from the 2021 EXport Processes in the Ocean from RemoTe Sensing (EXPORTS-NA) field campaign to assess the impacts of abiotic and biotic processes on the dynamics of marine snow. Using in situ determinations of aggregate particle size spectra and an array of supporting observations, we show that physical turbulence caused by springtime storms controlled the generation and destruction of marine snow in the mixed layer, as well as the timing of their export to depth. We also show that once these aggregates entered the relatively calm waters of the mesopelagic zone, biotic processes both consumed marine snow aggregates and transformed them into smaller particles, likely due to interactions with zooplankton.

2.0 The EXPORTS-NA Study Design and Data Used

2.1 Experimental Design, Sampling Array and Site Selection

The EXPORTS-NA field campaign was conducted ~150 km due east of the Porcupine Abyssal Plain (PAP) Observatory (Hartman et al. 2021) in the northeast Atlantic Ocean within a retentive anticyclonic eddy (Fig. S1; Erickson et al. 2023; Johnson et al. 2024). The siting within an anticyclonic eddy was to minimize the influence of spatial sources of variability on the temporal observations that were the aim of the study. Three research vessels (RRS *James Cook*, RRS *Discovery* & R/V *Sarmiento de Gamboa*), three instrumented gliders, an instrumented Lagrangian float and 10 water following surface drifters were deployed during the experiment. The location of the eddy center was monitored by analyzing available horizontal velocity measurements from the multiple sampling assets and verified by the Lagrangian float that remained near the eddy center throughout the study (Erickson et al. 2023). Measurements within 15 km of the analyzed eddy center were deemed to be in the eddy core based upon seawater property analyses. Below about 100 m, in the eddy core waters (ECWs), water parcels were retained within the eddy throughout the study (Johnson et al. 2024). Thus, changes in biogeochemical and ecological properties in the ECWs were due to local processes and were independent of changes due to horizontal advection. However, a series of four intense storms interrupted ship-based sampling (Fig. 1a), deepened mixed layer depths and exchanged significant fractions of the surface core waters (SCWs) due to Ekman transport (Johnson et al. 2024). The horizontal exchange fraction of surface core waters was the greatest during the first of the storms (73% of SCWs during the period, May 8 to 10). A full assessment of the physical oceanographic changes during the EXPORTS-NA field study is given by Johnson et al. (2024).

2.2 Data Used

The focus of this paper is the in situ determination of the particle size spectrum using Underwater Video Profilers model 5 (UVP; Picheral et al. 2010). The UVP illuminates approximately 1 L of seawater imaged at a pixel resolution of ~50 µm. Particles and aggregates are identified as contiguous pixels whose area is converted to equivalent spherical diameters (D_{esd}; which will hereafter be referred to as D). UVP deployments were made from each of the three ships, profiling from the surface down to at least 500 m. Excluding days with weather-related interruptions, 6 to 9 UVP profiles were made each day within the ECWs. Intercomparing the UVP data from the three ships, the range of particle sizes that can be reliably assessed ranged from a bin center of 0.13 mm to nearly 10 mm (Siegel et al. 2023b). Of particular interest in this study are marine snow aggregates, which are assessed by UVP imagery as a contiguous set of pixels with a D_{esd} larger than 0.5 mm. We also use the UVP data to assess the characteristics and dynamics of small particles ($0.13 \leq D \leq 0.5$ mm), as well as very large marine snow aggregates (MOUSs - Marine snow Of Unusual Size, *in sensu* D.P. Roberts), which we define as aggregates with $D \geq 5$ mm. Particle size spectra are reported as particle volume spectra in differential form (units are ppmV per mm bin width). This representation accentuates changes in the particle size spectra compared to visualizations made with particle abundance spectra. Data are presented here as 5 m vertical averages and each 5-m bin corresponds roughly to 100 L of seawater, given the UVP's sampling frequency and typical lowering rates. To help visualize changes in the largest marine show aggregates observed, we define the size of the largest particles robustly sampled by the UVP, D_{cdf}, as the diameter of the 95th percentile of the cumulative probability distribution of the particle volume spectrum. Further details on the processing of the UVP PSD data and calculations made using these data are provided in Section S2 of the *Supplementary Materials*.

Supporting measurements used here include vertical profiles of particulate organic carbon (POC), biogenic silica (bSi), particulate inorganic carbon (PIC), phytoplankton pigment and nutrient concentrations, zooplankton abundance and collections, sinking and suspended particles collected by marine snow catcher (MSC) deployments, ^{14}C-measured net primary production (NPP) rates, as well as sinking particle fluxes. Protocols for all measurements made during the EXPORTS-NA study are available at https://sites.google.com/view/oceanexports. Detailed methods for the supporting measurements used here are also presented in the *Supplementary Materials* section of this paper.

In the following, UVP imagery and supporting data will be used to assess marine aggregate characteristics and dynamics. These include the determination of aggregate porosity, calculation of coagulation and fragmentation rates for MOUSs, the assessments of zooplankton-marine snow encounter rates and the inverse modeling of mesopelagic metabolic rates and sinking speeds from the UVP observations. Complete background theory and calculation details for each assessment are presented in the *Supplementary Materials* section of this contribution.

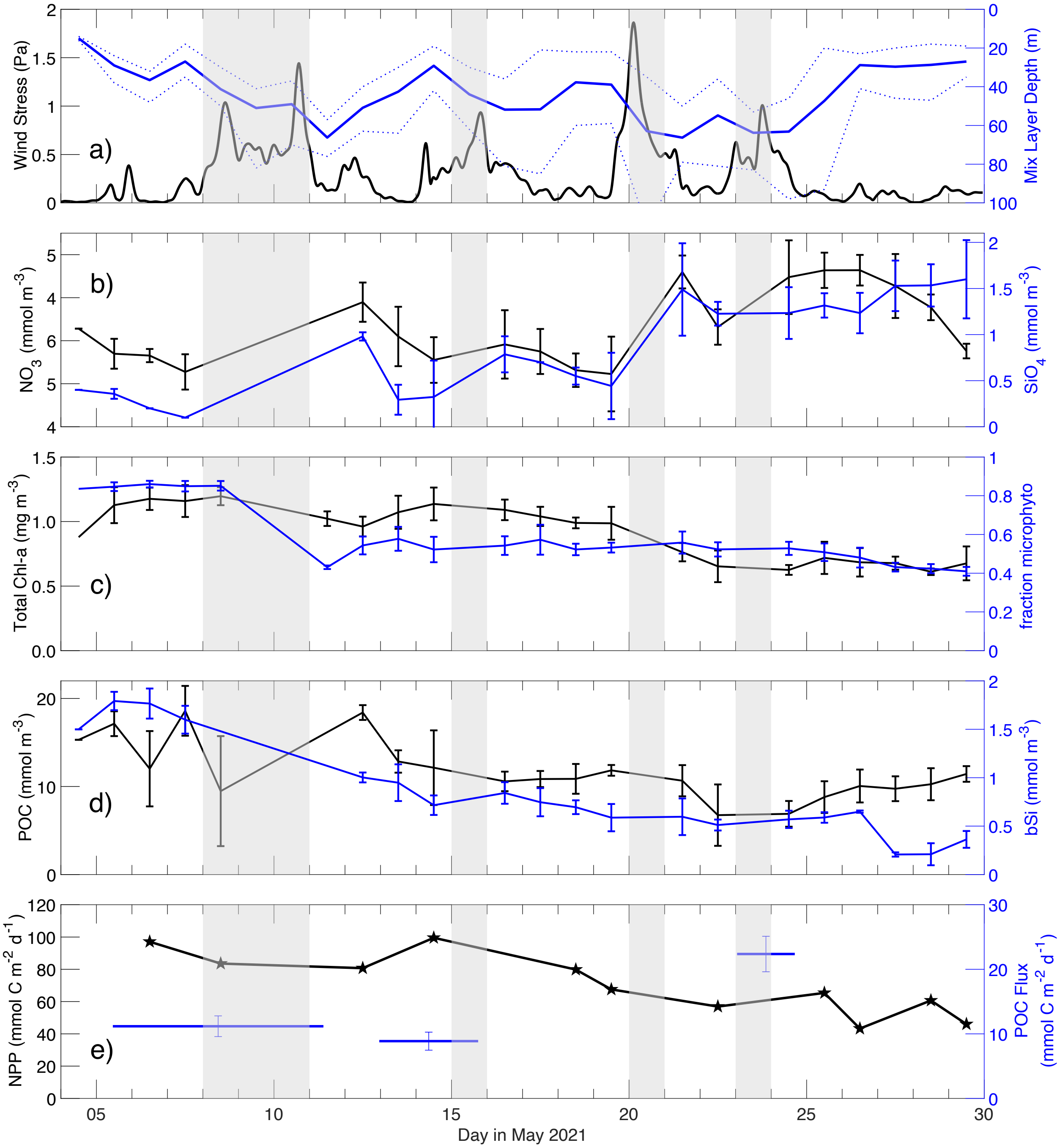

Figure 1: **Time series of oceanographic conditions in surface core waters during the EXPORTS-NA study**. Time series of a) wind stress (black; left axis) and daily minimum, mean and maximum mixed layer depth (blue; right), b) mixed layer mean nitrate (NO_3; black; left) and silicic acid ($Si(OH)_4$; blue right) concentrations, c) mixed layer daily averaged total chlorophyll *a* concentrations (black; left) and the contribution of diatom and dinoflagellate biomarker pigments to the weighted summed accessory pigment biomarkers (blue; right; following Uitz et al. 2006), d) mixed layer mean particulate organic carbon (POC; black; left) and biogenic silica (bSi; blue; right) concentrations and e) water column integrated rates of net primary production (NPP; black) and POC export fluxes measured at roughly 100 m using sediment traps (blue; right; see Table 1 for details). Length of the horizontal lines represent the trap collections times. All

measurements were made within 15 km of the eddy center. Error bars in panels b) to e) are standard deviation determinations for each daily mean or trap collection. Storm events when ship sampling was interrupted are indicated by the gray shading.

3.0 Results

3.1 The Oceanographic Setting

Initially, the surface core waters (SCWs) above the eddy center were characterized by extremely low silicic acid ($Si(OH)_4$) (<0.4 mmol m^{-3}), elevated nitrate (NO_3) (~5 mmol m^{-3}), moderate chlorophyll *a* concentration (~1.1 mg m^{-3}), and a dominance of microphytoplankton (as measured by the ratio of diatom and dinoflagellate biomarker pigment concentrations relative to the weighted sum of other accessory pigments; Uitz et al., 2006; Fig. 1). This combination of factors suggests that a bloom of diatoms had occurred previously and terminated due to Si limitation (Sieracki et al. 1993; Brzezinski et al. 2024). Analysis of the upper ocean silica and nitrogen budgets indicates that ~70% of the diatom bloom had already been exported from the mixed layer before our arrival (Brzezinski et al. 2024). The remaining nitrate supported the production of non-silicified phytoplankton during our field study, while storm-induced, mixed layer entrainment of dissolved silica concentrations supported intermittent diatom production (Fig. S2; Meyer et al. 2024; Brzezinski et al. 2024). This dual-phase bloom scenario is typical of the North Atlantic spring bloom (Sieracki et al. 1993). Thus, our focus here is on this second phase of the North Atlantic spring bloom and its associated particle export.

Table 1: Integrated POC and UVP Particle Volume Inventories and Sinking POC Fluxes During Trap Deployments

Trap deployment	Units	1	2	3
Dates		May 5-11	May 12-15	May 22-24
Water column integrated NPP	mmolC m^{-2} d^{-1}	119	120	53
Integrated POC	mmolC m^{-2}	829	812	788
POC Turnover Time by NPP	day	7.0	6.7	14.9
Trap Type & Depth		75 m STT	75 m STT	109 m NBST
POC export	mmolC m^{-2} d^{-1}	11	9	22
e-ratio	-	0.09	0.07	0.42
POC Turnover Time by Export	day	75	90	36
Integrated Particle Volume	ml m^{-2}	421	1366	1279
Integrated POC / Particle Volume	mmolC / ml	1.97	0.59	0.61
Trap BSi / POC Fluxes	mol Si / mol C	0.10	0.28	0.26

Notes: Determinations of water column integrated NPP rates from Table 1 in Meyer et al. (2024) are averaged over the periods of the three trap deployment periods. Integrated POC stocks were calculated from available POC profiles water samplings profiles and again averaged over the periods of the three trap deployments. Trap-derived POC export fluxes were determined using the shallowest depths available. E-ratios are calculated as the POC export flux at the upper trap depth (10-11 m beneath the 0.1% PAR depth in deployments 1-2, and 28 m below in deployment 3) normalized by the NPP. Particle volume inventories during the trap deployments were integrated over the upper 100 m. STT is surface tethered trap array and NBST is Neutrally Buoyant Sediment Trap.

Most SCW biogeochemical variables were highest upon arrival at the eddy and decreased over time. These variables included: chlorophyll *a*, POC, bSi, the relative contribution of microphytoplankton pigments to accessory pigments, and water column integrated NPP rates (Fig. 1cde; Johnson et al. 2024; Brzezinski et al. 2024; Meyer et al. 2024). Notably, vertically integrated rates of NPP decreased by nearly a factor of two during the study. The first storm event (May 7-11) had a large impact on the retention of SCWs and ~75% of these SCWs were exchanged with waters from outside of the eddy core region, while daily mean mixed-layer depths deepened from 22 to 68 m (Johnson et al. 2024).

While NPP decreased two-fold over the course of the study, upper ocean sinking POC fluxes increased two-fold from the first to the third sediment trap deployments (Fig. 1e; Table 1). Comparing the POC flux at roughly 100 m to the POC stocks above it provides a measure of turnover of POC due to export from the upper ocean. These export turnover times were 2 to 3 months during the first two sediment trap deployments and about one month for the last (Table 1). Turnover times for the production of POC (defined as POC inventory / NPP) were considerably shorter (1 to 2 weeks; Table 1), illustrating that much of the fixed organic carbon was utilized by the upper ocean ecosystem and not exported to depth. However, both lines of evidence suggest a residence time of upper ocean POC stocks of ≥1 week.

3.2 Observations of Large Particles and Marine Snow Aggregates

Abundance-size distributions of large particles (~0.1 to 10 mm) were quantified as a function of depth and time using the three UVPs. Figure 2a shows selected daily mean vertical profiles of differential particle volume spectra sampled within 15 km of the eddy center. Initially, high volume concentrations of particles with D < 1 mm occurred in the mixed layer while comparatively lower particle volume concentrations of any size were found at depth. From May 12-16, the maximum sizes of particles observed in the mixed layer increased to > 3 mm, which may have been caused, at least in part, by horizontal exchanges of surface waters due to the storm-induced Ekman transport (Johnson et al. 2024, San Soucie et al. 2024). After May 15, a plume of large marine snow particles (> 3 mm) appeared beneath the ML and over the next several days sank into the ECWs. By May 25, the plume of large particles reached 500 m, implying an average sinking speed of ~33 m d^{-1} (300 m over 9 d). Post-bloom ecosystems in the North Atlantic often lead to rapid export of sinking particles from the surface ocean, but the time lag between the first appearance of these particles in and just beneath the SCWs and their export was unexpected.

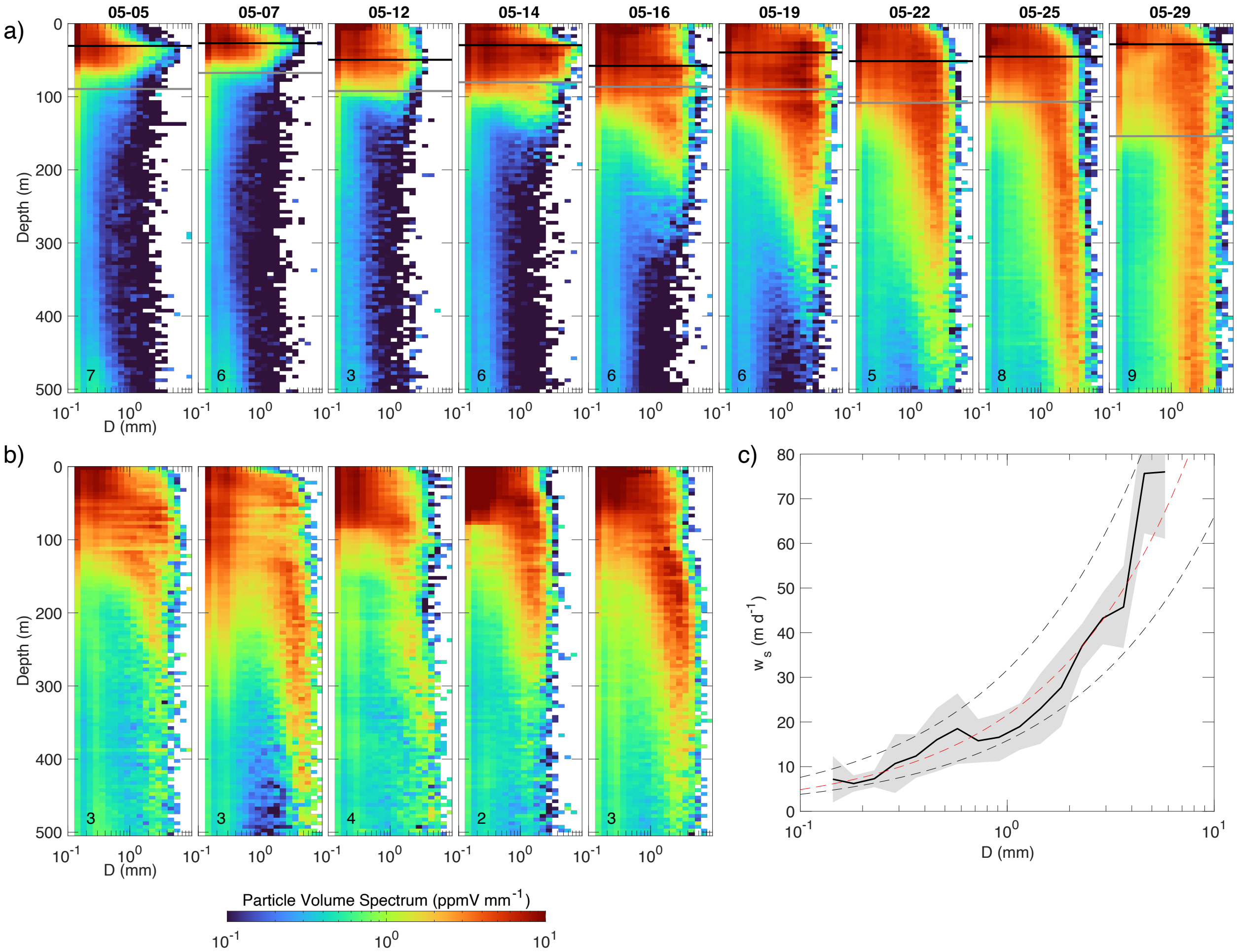

Figure 2: **Vertical profiles of the particle volume size distribution for selected days**. a) Daily mean, differential particle volume spectra (ppmV mm^{-1}) profiles for selected days during the cruise and within 15 km of the eddy center. Particle volume spectra are presented in differential form to accentuate changes in the particle size spectra that are difficult to visualize using particle abundance spectra. Particle sizes were measured in equivalent spherical diameters (ESD) which are logarithmically distributed with bin centers from 0.13 to 10.3 mm. The black line denotes the daily mean MLD near the eddy center, while the gray line denotes the depth of the daily mean 27.2 kg m^{-3} isopycnal, which defines the upper boundary of the ECW (Johnson et al. 2024). Storm events disrupted ship-based sampling on May 9-10, 15, 20 and 23 (see Fig. S3 for the complete daily mean time series). The number in the lower left corner of each spectrum profile is the number of UVP casts used to create each daily mean spectra. b) Daily mean particle volume spectra (ppmV mm^{-1}) profiles outside the eddy (15 to 60 km from eddy center) for days corresponding to the first 5 days selected in panel a. c) Study mean particle sinking speed ($w_s(D)$) size distribution from following UVP particle abundance isosurfaces in time (black solid line; see Suppl. Section S3). The standard deviation of the sinking speed estimates (gray shading), a fit through the mean values ($w_s(D) = 20.2\ D^{0.67}$; red dashed line) and two widely applied $w_s(D)$ estimates (dashed lines) from Kriest (2002) (entries 8

& 9 in Table 2 in their paper) are also shown. Further details are provided in Supplemental Sections S2 and S3.

During the first 10 days of the study, daily mean particle volumes within the ECWs (≥ 100 m) were relatively low and dominated by smaller particle sizes (Fig. 2a). However, outside of the eddy core at similar depths, substantially more and larger particles were observed at the same depths (Fig. 2b). In particular, the particle volume spectra profiles seen outside of the ECWs during the first half of the study were similar to those observed later within the ECW (after May 22; Fig. 2a). This observation suggests that the midwater environment outside of the eddy core had already been modified by the passage of sinking particle plumes, while this signal was initially absent within the ECWs. At these depths, the water column outside the ECW was likely enhanced by lateral mixing from a patchwork of export flux events, as demonstrated by the high degree of spatial heterogeneity in the surface biological fields, and as can be seen in daily mean satellite chlorophyll distributions (Fig. S1). The low abundance of large particles within the ECWs observed initially confirms the high degree of water parcel retention in the anticyclone's ECW (Johnson et al. 2024) and indicates that there had not been a recent export flux event above the eddy core waters although there had been in the waters outside of the eddy. Importantly, the initial low particle volumes in the ECW suggests that the ECWs are a nearly pristine environment for diagnosing the dynamical relationships among particles and sinking particle fluxes.

3.3 Estimation of the Size Spectrum of Particle Sinking Speeds

The sinking speed estimate suggested from the large particle plume can be refined to assess sinking speed as a function of particle size. Here, the sinking speed size distribution, $w_s(D)$, is determined by assessing temporal changes in the depth of particle abundance isosurfaces for each size bin following Lacour et al. (2023) (see Suppl. Section S3). Values of $w_s(D)$ increased with size and ranged from roughly 7 m d^{-1} to ~75 m d^{-1} for the largest particles assessed (Fig. 2c). A power-law fit through the mean curve vs. diameter results in $w_s(D) = 20.2\ D^{0.67}$. The retrieved $w_s(D)$ values correspond well with theoretically derived sinking speed size distributions for marine snow (Kriest, 2002).

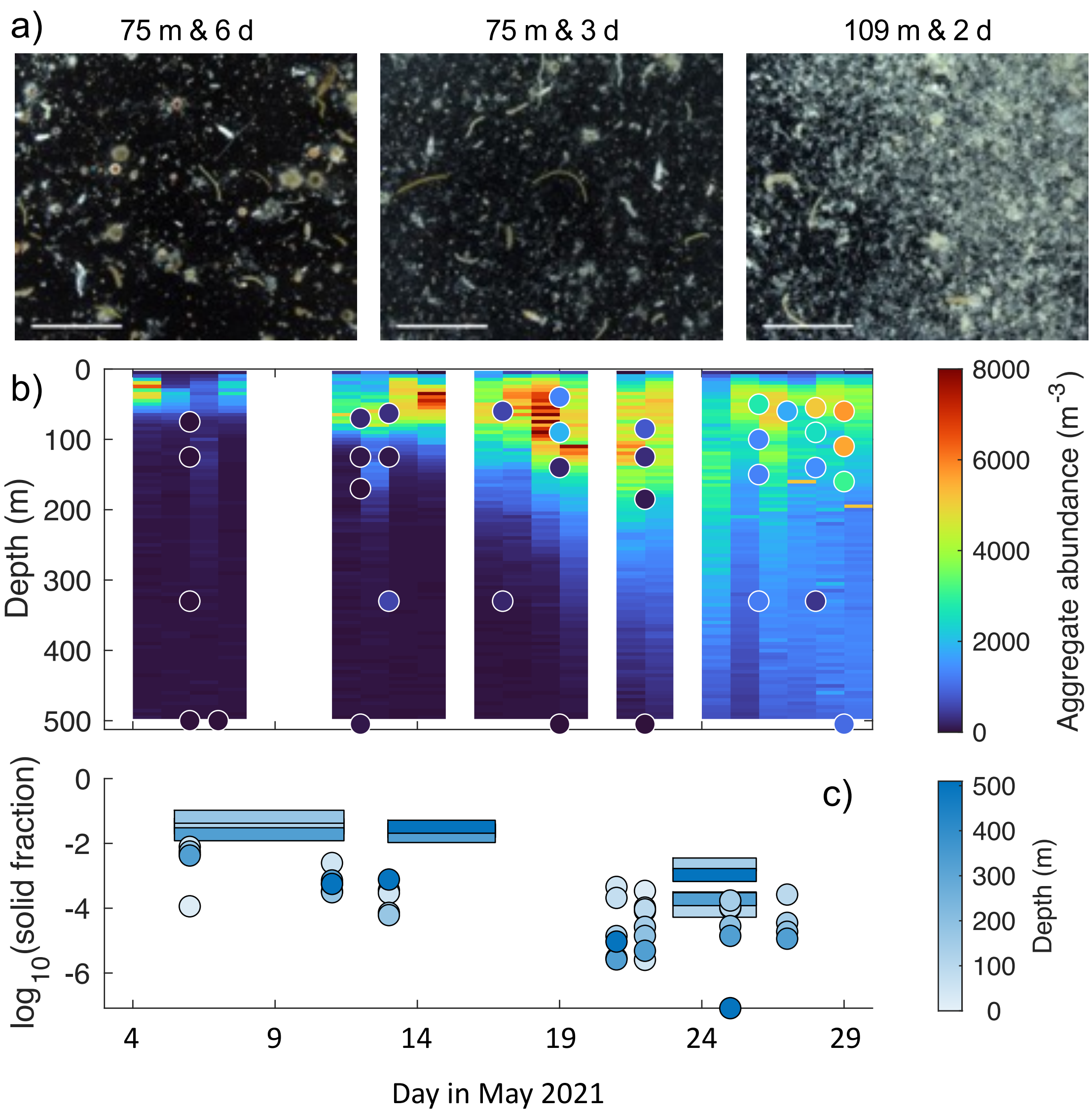

Figure 3: Structural changes in large particle characteristics in time and depth. a) Representative micrographs of gel trap contents from the three shallowest sediment trap deployments during the cruise (see Table 1). Scale bars in lower left corners of images (red) are 1 mm in length. Sampling depths of the 3 sediment trap collection periods were 75 m, 75 m, and 105 m. Notably, trap sampling durations decreased during the cruise from 6 days, to 3 days, to 2 days. b) Aggregate abundance and composition determinations as function of depth and time within the eddy center. UVP-imaged aggregate abundance analysis are shown in the heat map, while fast sinking, large aggregates hand collected from the MSC collections are the filled circles. c) Solid particle fractions from geochemical/gel trap pairings (rectangles for which length denotes the trap collection duration) and near-simultaneous high-volume pump and UVP observations (circles). Depth of sample collections is shown in the color scale. Relevant measurement and analysis methods can be found in Supplementary Sections S4 and S5.

3.4 Structural Characteristics of Marine Snow Aggregates

Knowing the physical structure of a particle is important for assessing its interactions with the environment and the organisms therein (Burd and Jackson, 2009; Laurenceau-Cornec et al. 2015; Iversen, 2023). Micrographs of sediment trap contents (Fig. 3a) show that large particles increased in number, size, and porosity over the duration of the cruise. These findings were corroborated by marine snow catcher (MSC) observations of modest increases in aggregate abundances after May 18, with a higher number and larger volume of fast-sinking aggregates over time and with depth (Fig. 3b; Romanelli et al. 2024). Peak aggregate abundances observed from the MSC collections occurred on May 29, four days after the last sediment trap deployment. Daily mean aggregate abundances determined via automated classification of the individual UVP vignette images were roughly consistent with the MSC results (Fig. 3b; Drago, 2023). However, peak abundances of the UVP-imaged aggregates occurred on May 18, well before the peak concentrations were observed from the MSC collections. Overall, more than 90% of the particles larger than 1 mm characterized from the individual UVP images were identified as aggregates (Drago, 2023).

Large particles were extremely porous throughout the time series, with solid particle fractions (defined as 1–porosity) ranging from 10^{-2} to 10^{-6} (Fig. 3c), similar to the range of solid particle fractions found in previously reported in situ field determinations (Alldredge and Gotschalk, 1988). Particle solid fractions were estimated by two methods: from sediment trap samples that collected sinking particles and from large volume pump-UVP pairings that sampled particles from the water column (Supplementary Section S5). Determinations of the solid particle fraction were higher for the sinking particles captured in traps than for particles imaged in the water column, as expected. Both estimates of solid particle fractions decreased over time, but no obvious changes with depth were found (Fig. 3c). The increase in porosity can also be seen in the more than three-fold decrease in the suspended POC concentrations normalized by the UVP-determined total particle volume integrated over the upper 100 m (Table 1).

Changes in the chemical composition of the sinking particles was also observed. For example, the biogenic silica to POC ratio composition of the sinking particles collected by the sediment traps at the base of the euphotic zone increased by more than a factor of 2 from the first to the second trap deployment (Table 1). An increase in bSi to POC ratios is also seen in the marine snow catcher collections of small sinking particles (Romanelli et al. 2024).

3.5 Abiotic Controls on Marine Snow Distributions in the Mixed Layer

The observations of particle size distribution revealed several instances where physical processes had the dominant controls on the dynamics of marine snow particles. For example, daily mean UVP profiles showed large reductions in the volume of particles for a given size bin near the sea surface (Figs. 2a). This result suggests that upper ocean turbulence may have an important role on the present observations of the size and abundance of marine snow particles.

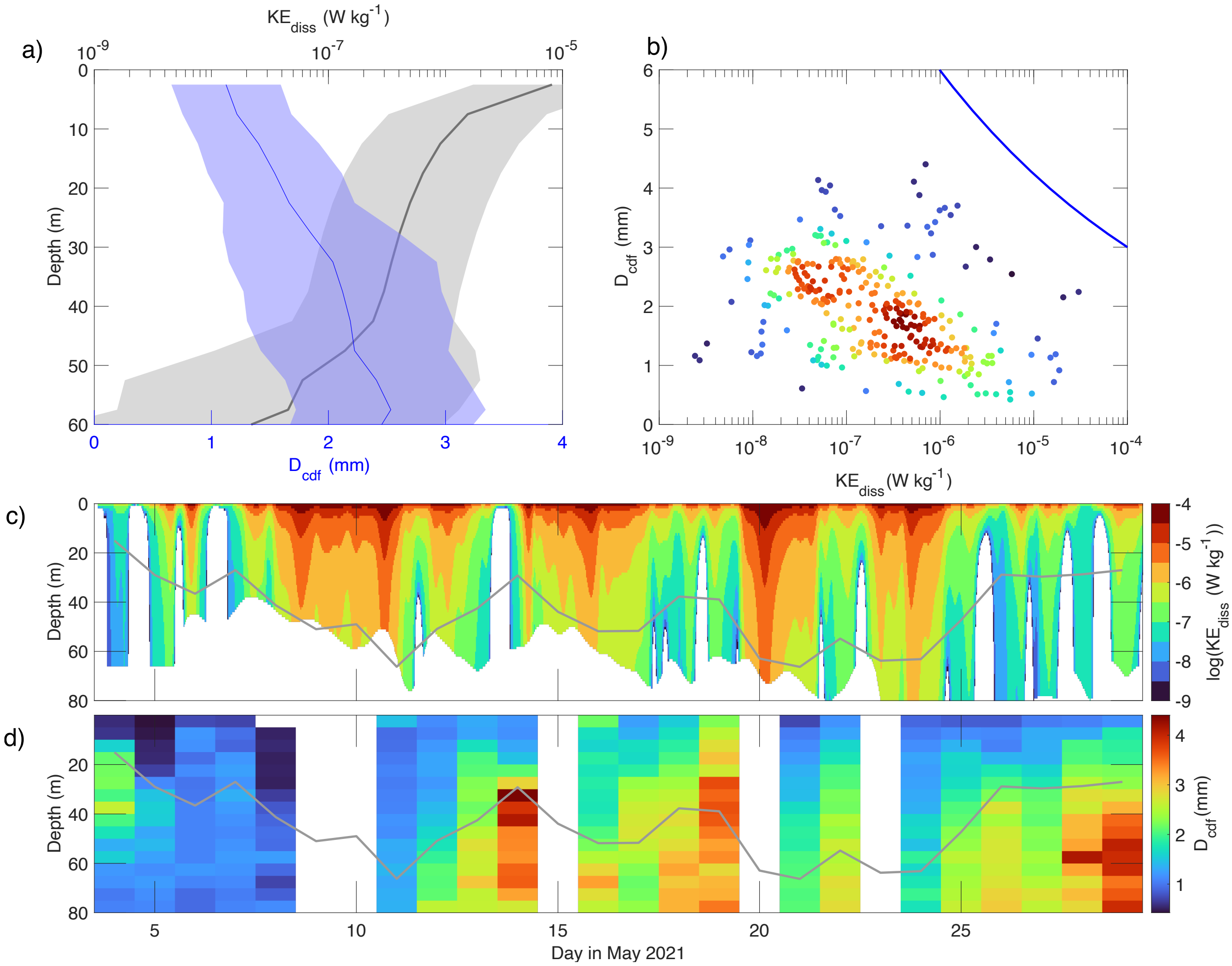

Figure 4: Mixed layer turbulence and the largest particle sizes observed. a) Study mean profiles of the largest particle size robustly sampled by the UVP (orchid line & shading), D_{cdf}, and the KE_{diss} turbulent kinetic energy dissipation rate (gray line & shading), KE_{diss}, estimated from air-sea momentum and buoyancy fluxes. Data were only considered if they were in the mixed layer and the shaded envelopes represent the standard deviation about the mean. b) The relationship between coincident daily mean D_{cdf} and KE_{diss} observations found within the mixed layer. Blue line is a relationship determined from the experiments of Alldredge et al. (1990) (D_{max} = 0.75 (KE_{diss})$^{-0.15}$). Data points are colored to represent the data density in D_{cdf}-KE_{diss} space (redish shades the highest and violet lowest). c) Depth-time distribution of hourly KE_{diss} estimates in the upper 75 m. The gray line is the daily mean depth of the mixed layer from an instrumented glider which profiled approximately every two hours near the eddy center (Johnson et al. 2024). d) Daily mean depth-time distribution of the largest particle size metric, D_{cdf}, with the daily mean mixed layer depth (gray line). Methodological details are provided in Supplementary Sections S2, S6 & S9.

The size of the largest particles reliably sampled by the UVP (D_{cdf}) showed a clear correspondence with the intensity and vertical distribution of mixed layer turbulence

(Fig. 4a). Mean values of D_{cdf} increased with depth within the mixed layer by more than a factor of two, while study mean estimates of the turbulent kinetic energy dissipation rate, KE_{diss}, decreased by many orders of magnitude, from nearly 10^{-5} W kg^{-1} to < 10^{-7} W kg^{-1}. The signal of turbulence on the sizes of marine snow aggregates is also seen in comparison of daily mean D_{cdf} and KE_{diss} values within the mixed layer (Fig. 4b). Overall, a weak but significant negative relationship was observed between D_{cdf} and $\log_{10}(KE_{diss})$ ($R^2 = 0.14$, $p<0.01$, N=303), supporting the notion that mixed layer turbulence limits the size of the largest marine snow particles. All D_{cdf} values remained below maximum aggregate sizes typically found in the laboratory experiments of Alldredge et al. (1990) (blue line in Fig. 4b). As the D_{cdf} metric is defined as the 95th percentile of the observed particle volume distribution, it cannot measure the size of the very largest particle.

The two-fold increase in the largest particle sizes, D_{cdf}, with depth also provides insights into the dynamics of marine snow aggregates. Classic turbulence scaling predicts mixed-layer turnover times of an hour or less (scaling as Z_{ML} / u^*, where Z_{ML} is the mixed-layer depth, u^* is the surface friction velocity = $(\tau/\rho)^{1/2}$; τ is wind stress and ρ is seawater density). Thus, the maintenance of a vertical gradient in D_{cdf} in the face of rapid mixing in the upper ocean mixed layer indicates that the process of shear fragmentation of aggregates must have occurred very quickly, with time scales of much less than an hour (maybe instantaneously). These data also show that the largest particle sizes were found for intermediate values of KE_{diss} (Fig. 4b). This result suggests that there is a turbulence level, roughly 10^{-7} W kg^{-1}, that is large enough to promote particle-particle encounters leading to coagulation, but not so large as to lead to disaggregation of those particles.

Throughout this study, estimates of KE_{diss} within the mixed layer varied by more than four orders of magnitude as a function of both depth and time (Fig. 4c). The highest KE_{diss} estimates were near the sea surface and increased over time throughout the mixed layer due to the passage of storms. Reflecting this trend, the size of the largest particles, D_{cdf}, varied accordingly, increasing when turbulence levels were low and decreasing dramatically as the storms passed (Fig. 4d). The daily increases in D_{cdf} within the mixed layer were evident between May 11-14 and May 16-19. Simultaneously, total particle volumes increased nearly two-fold during these times (Fig. 5a). The large temporal changes in upper layer total particle volume appeared to be largely independent of changes in NPP rates (Fig. 1e) or suspended POC stocks (Fig. 1d), indicating that changes in particle size (and possibly porosity), not particle mass, were regulating the rapid changes in total particle volumes. Changes in the upper-layer mean particle volume size spectra mirrored changes in the turbulence levels where particle sizes and volumes grew when turbulence levels were low and decreased when turbulence was high (Fig. 5b). In fact, the mean relationship found by Alldredge et al.

(1990) appears to be an effective description of upper bound for the size of marine snow aggregates.

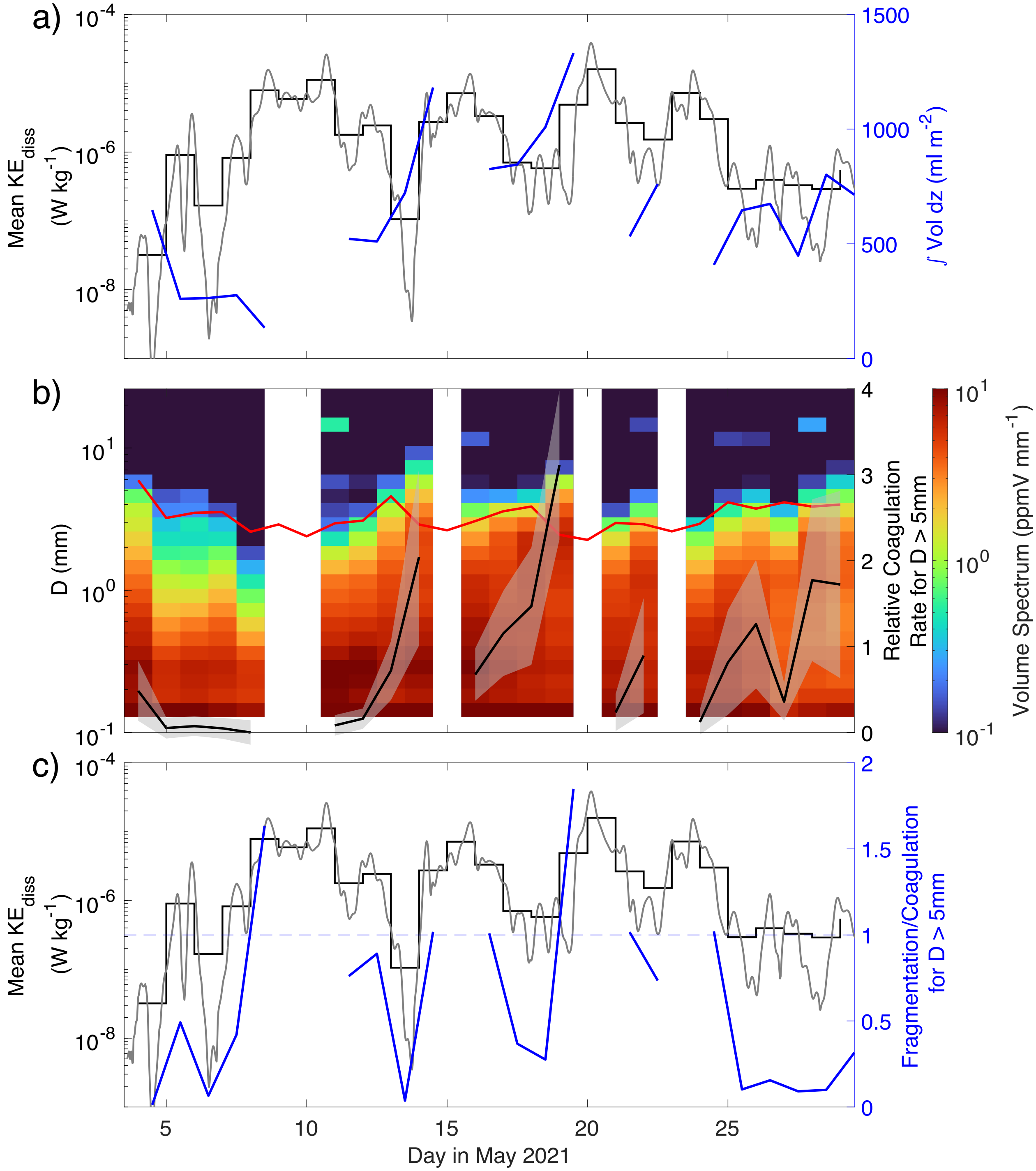

Figure 5: Upper layer marine snow particle dynamics. a) Integrated particle volume time series averaged over the upper 50 m is displayed on the right axis. The left axis shows the time evolution of the mean KE_{diss} in the upper 50 m (black; hourly & daily). b) Upper 50 m mean particle volume spectra as a function of time. Black lines are modeled time series of relative coagulation rates for the largest marine snow aggregates (MOUS's; D > 5 mm) in the upper 50

m. The uncertainty envelope for coagulation rates illustrates the variations in the ensemble created using a range of fractal dimension scenarios. Also plotted (red line) is the maximum marine snow size as function of upper layer KE_{diss} based upon the laboratory experiments of Alldredge et al. (1990). c) Time evolution of the mean KE_{diss} in the upper 50 m (left axis, black; hourly & daily) and the ratio of modeled particle fragmentation to particle growth via coagulation for particles larger than 3 mm (right axis, blue line; > 1 fragmentation dominates and < 1 coagulation). Methods for assessing marine snow coagulation and disaggregation rates are presented in Supplementary Sections S7, S8. and S9.

The highly ephemeral nature of the largest marine snow aggregates is reflected in temporal patterns of normalized formation rates of marine snow of unusual size (MOUSs; D>5 mm) (Fig. 5b). Initially, upper-layer shear coagulation rates were nearly zero due to both low turbulence levels and a scarcity of aggregates that could coagulate into very large marine snow aggregates. After each storm, normalized particle coagulation rates increased from near zero to more than two as there was sufficient turbulence to promote coagulation and particles were large enough to produce MOUSs at significant rates. However, if particles became too large and the turbulence levels were high enough, particle fragmentation occurred (Fig. 5c). In fact, the dynamics of MOUSs was driven by fragmentation when turbulence was high (upper layer mean KE_{diss} greater than 3×10^{-7} W kg^{-1}) and coagulation when turbulence levels were lower (Fig. 5c). Together, these data illustrate the highly ephemeral nature of large aggregates in the upper ocean as perturbed by moderate to intense storm conditions.

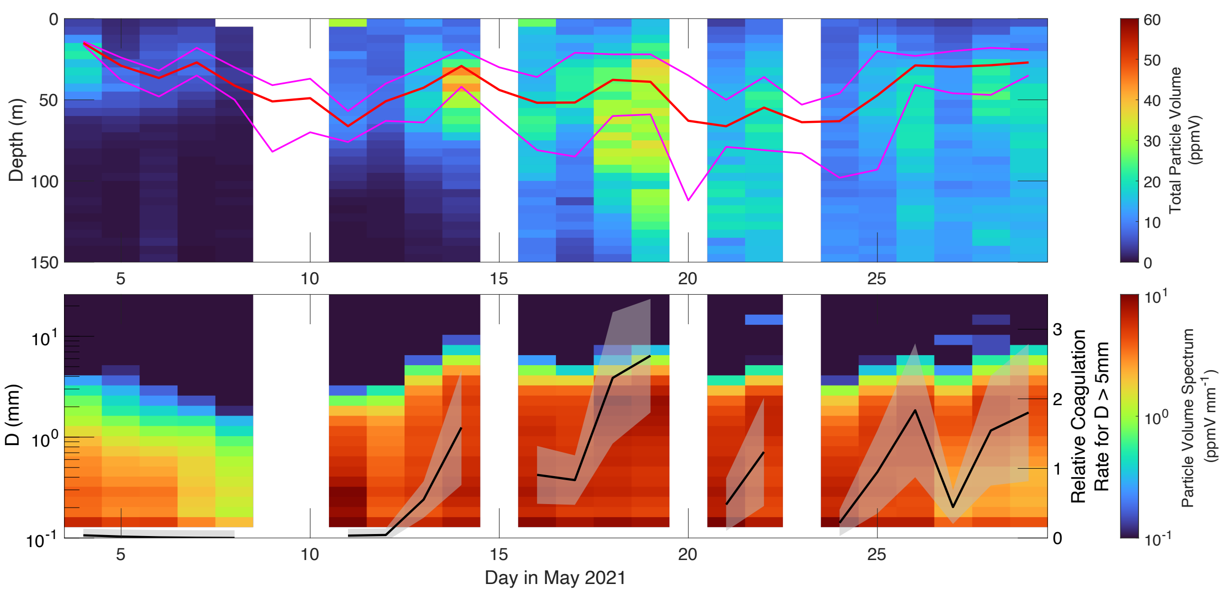

Figure 6: Mixed layer pumping of large particles at depth due to the successive storms. a) Total particle volume depth-time series from the UVP- particle imagery (ppmV). Daily mean (red), minimum (lower pink line) and maximum (upper pink line) mixed layer depths from the instrumented glider are shown. b) Daily mean particle volume spectrum averaged for the layer between 40 to 80 m as a function of particle size. Overlaid are modeled time series of relative coagulation rates for marine snow of unusual size (MOUSs; D > 5 mm) in the same layer. The uncertainty estimates are calculated over the ensemble of different fractal dimension scenarios.

3.6 Roles of Mixed Layer Dynamics on the Timing of Sinking Particle Fluxes

The succession of storm events also influenced marine snow dynamics by rapidly altering the depth of the surface mixed layer, which in turn impacted the vertical transport of marine snow to depth. As noted above, a pulse of sinking particles was observed traversing the mesopelagic from the base of the mixed layer starting on May 14 and reaching 500 m on about May 25 (Fig. 2a). However, it is not obvious what drove the timing of the sinking particle flux event.

Initially (May 6-9), the UVP-imaged total particle volumes were very low just beneath the mixed layer (Fig. 6a) and the 40 to 80 m averaged particle volume spectra showed very few particles that were > 1 mm (Fig. 6b). The first storm not only exchanged some of the eddy's surface waters with waters from outside, but it also deepened the daily mean mixed layer from 22 to 68 m (Fig. 6a). After operations resumed on May 11, particle abundances and sizes near the base of mixed layer (40-80 m) were more than four-fold larger, likely due to vertical mixing and particle sinking. During the calm period between the first two storms (May 11 through 14) within the 40 to 80 m layer beneath the mixed layer, total particle volumes increased by a factor of more than two (Fig. 6a). This trend was also reflected in the largest particle size metric, D_{cdf}, which grew nearly four-fold (Fig. 4d). The temporal patterns in the relative coagulation rates for the 40 to 80 m layer of MOUS aggregates support the idea that shear coagulation was a driver of this increase in this depth range (Fig. 6b). The mixed layer also shallowed by nearly 30 m during this calm period (Fig. 6a), effectively exporting marine snow particles beneath the shallowing mixed layer in a process similar to the mixed layer carbon pump (Gardner et al. 1995; Dall'Olmo et al. 2016). This physically driven export of marine snow was enhanced by particle sinking as the largest particles were sinking at ~75 m d^{-1} (Fig. 2c).

This process was repeated after the second storm end, but this period (May 16 to 19) started with larger and more numerous aggregates (Fig. 6b). These increases were reflected in the roughly two-fold increase in relative coagulation rates for the 40 to 80 m layer of MOUSs compared with the previous calm event. During this second calm period (starting roughly May 16), the plume of large particles was observed sinking to depth (Figs. 2a & 6a). Thus, the large observed export pulse of marine snow resulted from a complex combination of processes, including mixed layer entrainment and detrainment transporting large particles to depth, shear coagulation creating larger particles that were isolated from the high KE_{diss} rates near surface, and finally the rapid sinking of those large particles into the eddy interior.

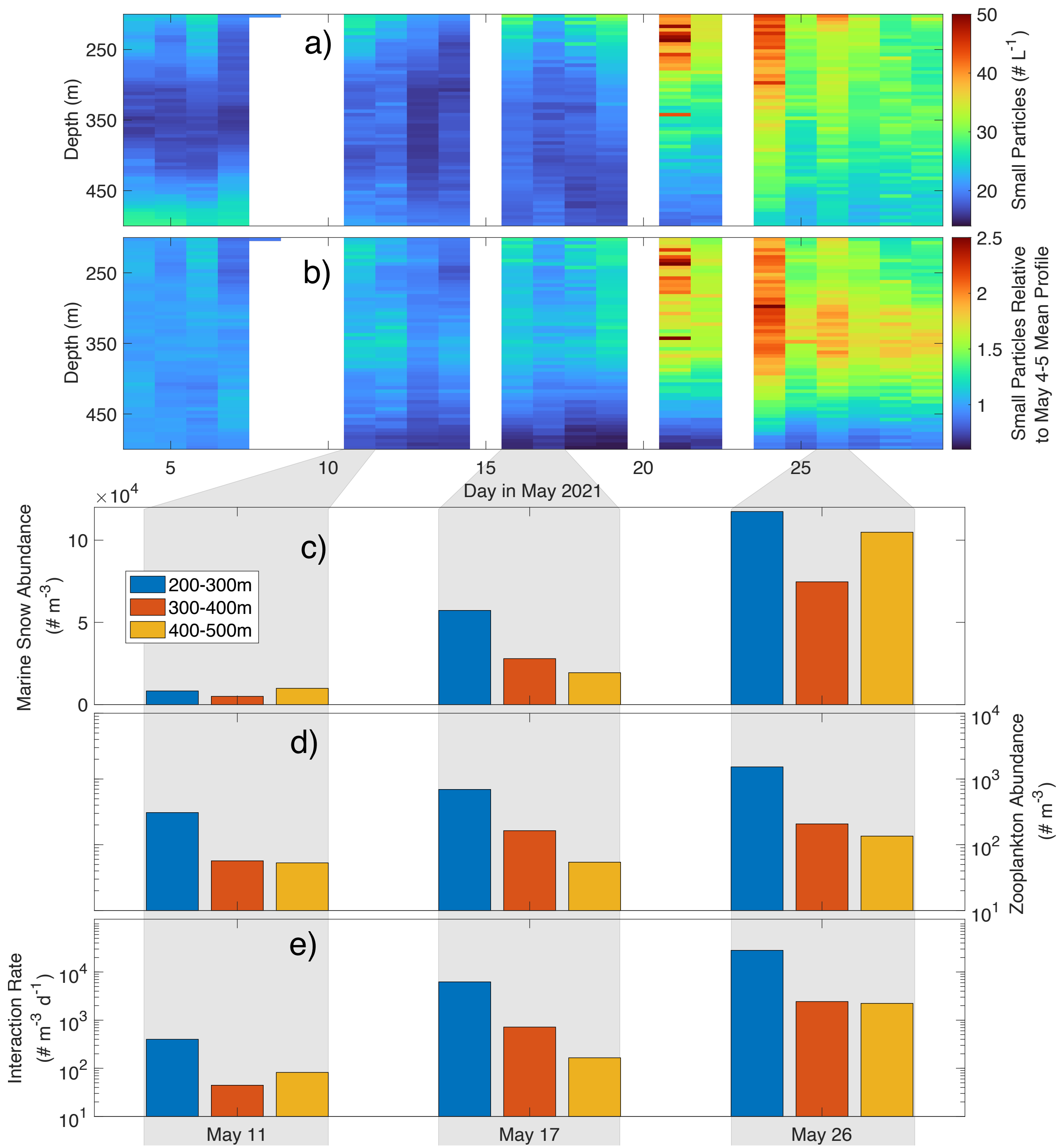

Figure 7: **Changes in small particle abundances in the mesopelagic.** a) Abundances of particles imaged that were smaller than marine snow (0.13 > D > 0.51 mm) plotted as a function of depth and time. b) Relative changes in the vertical profile of the abundances of particles smaller than marine snow (0.13 > D > 0.51 mm) with depth and time relative to the mean profile from May 4 and 5. c) Abundances of marine snow particles (D ≥ 0.51 mm; units of # m^{-2}) for the days May 11, 17 & 26 averaged over depth bins between 200 and 300 m (blue), 300 and 400 m (red) and 400 to 500 m (gold). d) Abundances of zooplankton for the same depths and dates as panel c. e) Marine snow-zooplankton encounter rate (# interactions m^{-3} d^{-1}) calculated using Eq. S8. Supplemental section S10 provides details of the encounter rate calculation.

3.7 Controls on Marine Snow in the Upper Mesopelagic

The controls on the marine snow dynamics in the upper mesopelagic zone (200 to 500 m) of the eddy core waters can also be quantified using the present observations. After May 20, abundances of small (≤ 0.51 mm) particles within the ECW increased by a factor of 50 to 100% compared to May 4-5 (Fig. 7a). It is unlikely that these smaller particles sank from the surface ocean given the time required for these slowly sinking particles to traverse many hundreds of meters (Fig. 2c). Horizontal advection or mixing can also be ruled out due to the retentive nature of the eddy core waters. Further, shear disaggregation can be ruled out, as KE_{diss} levels are will be far too low at these depths ($< 10^{-9}$ W kg^{-1}; Franks et al. 2022). More likely, the observed increase in small particles was driven by biological processes, such as the destruction of marine snow particles by zooplankton via sloppy feeding and/or animal-generated shears (Dilling and Alldredge, 2000; Steinberg and Landry, 2017).

Support for this hypothesis can be found in determinations of the encounter rates between sinking marine snow and zooplankton. Encounter rates, within the ECWs below 200 m, are modeled as the product of the zooplankton and marine snow abundances, the marine snow sinking speed, and a length scale over which a zooplankter can sense a sinking particle (see Supplemental section S10 for details of the encounter rate model and its application). For the three days where simultaneous zooplankton abundance profiles and UVP imagery data were available near the eddy center, modeled encounter rates increased by more than 25-fold from May 11 to May 26 (Fig. 7e; Table S1). These increases were due to large increases in both zooplankton and marine snow abundances (Fig. 7c & d). The timing of the large increase in encounter rates is consistent with the suggestion that the transformation of marine snow by zooplankton created these smaller particles.

The UVP-imaged particle observations can be used to quantify the fate of marine snow within the mesopelagic using a two size-class model (Eq. 1). The model relates the time rate of change of small (V_S: $D < 0.51$ mm) particle and marine snow (V_L) conserved volumes to the sum of their respective sinking speeds through the water column (w_S & w_L), the transformation of marine snow to small particles with a specific rate β, and the consumptive losses of each with a specific rate γ, or

$$\frac{\partial V_S}{\partial t} = w_S \frac{\partial V_S}{\partial z} + \beta V_L - \gamma V_S \quad \text{(1a)}$$

$$\frac{\partial V_L}{\partial t} = w_L \frac{\partial V_L}{\partial z} - \beta V_L - \gamma V_L \quad \text{(1b)}$$

Model coefficients were estimated via linear least squares using determinations of the conserved volumes (and their gradients in depth and time) of V_S and V_L from daily mean observations within the ECWs using data for depths between 200 and 500 m. An ensemble of fractal dimensions was created, as these values are uncertain, which also provided a range of retrievals for uncertainty estimation (uncertainty estimates are given in the values in parentheses in Table 2). The conversion of the UVP observed particle volumes to conserved volumes is required to ensure that particle masses are preserved under transformations (see Supplementary Section S7). Calculation details for the determination of the model coefficients in equation 1 can be found in Supplementary Section S11.

Table 2: Inverse Modeling of Particle Fates in the Mesopelagic

Parameter	Symbol	Units	Mean & Standard Deviation	
Model			**Constant w_L**	**Time-varying w_L**
Small Particle Sinking Speed	w_S	m d^{-1}	12.1 (1.6)	20.9 (2.3)
Marine Snow Sinking Speed	w_L	m d^{-1}	68.9 (2.7)	1.18 (0.4) * day + 47.2 (9.1)
Particle Consumption Rate	γ	d^{-1}	0.118 (0.008)	0.122 (0.010)
Marine Snow to Small Particle Transformation Rate	β	d^{-1}	0.010 (0.006)	0.008 (0.006)

Ensemble means for the model coefficients along with uncertainty estimates (reported as the ensemble's standard deviation) are reported in Table 2. Retrievals for the particle consumption rate (γ) are ~12% per day, indicating that there was a substantive loss of particles as they sank through the mesopelagic (Table 2). The transformation rate of large to small particles (β) was considerably smaller than the consumption rates (~1% per day), yet positive for all ensemble members, demonstrating that there was a net production of small particles from large ones. The retrieved sinking speeds for large and small particles were consistent with the retrievals made following particle abundance isosurfaces (Fig. 2c). Finally, the particle transformation model coefficients (γ and β) were similar whether or not a time dependence was assumed for the sinking rate of marine snow (w_L; Table 2).

4. Discussion

The results presented here assess the evolving distributions of marine snow particles during the decay of a North Atlantic spring bloom. We show the important role of storm-induced turbulence in the near-surface mixed layer on particle distributions, their characteristics and the links to sinking particle fluxes. We also quantify the roles that biotic processes have in creating and destroying marine snow particles in the mesopelagic zone using an inverse model. A conceptual diagram of these coupled processes during our study is shown in Figure 8. In the following, we discuss the abiotic vs. biotic controls on sinking marine snow particles, impacts of the changes in the characteristics of marine snow, and consider the multifaceted roles of marine snow dynamics in observational and modeling studies of the functioning of the ocean's biological carbon pump.

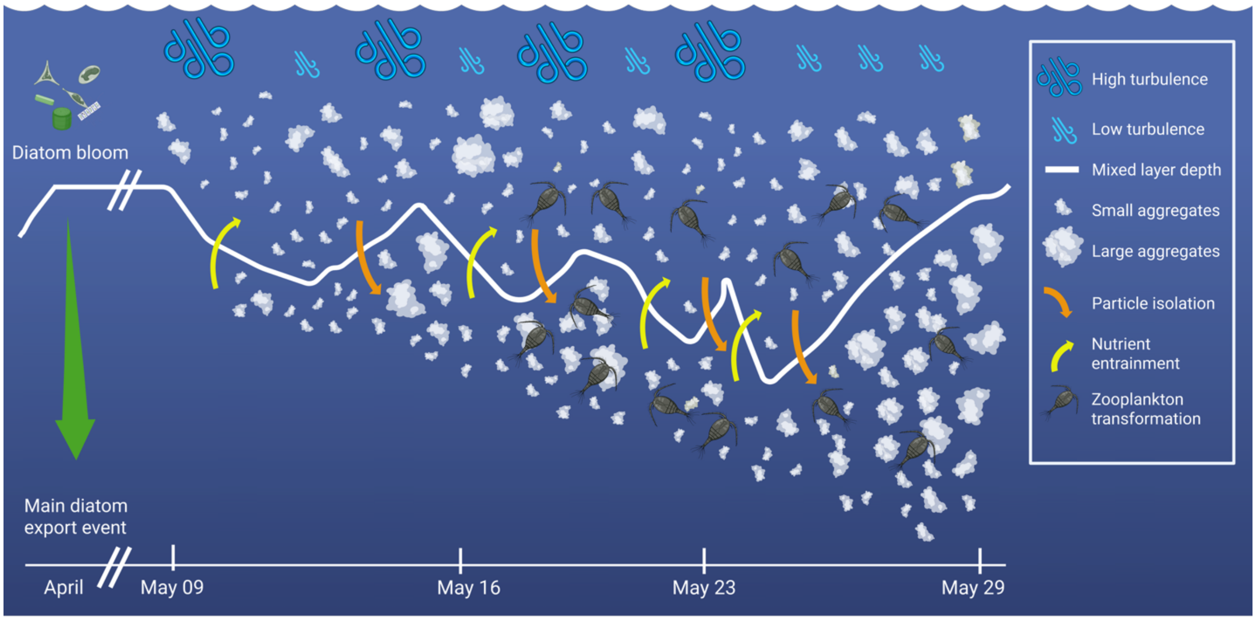

Figure 8: **Conceptual diagram of the observed marine snow dynamics during the EXPORTS-NA study.** Diagram illustrates the time-depth distribution and dynamics of marine snow aggregates, their response to the sequence of storm events, interactions with zooplankton and sinking to depth.

4.1 Impacts of Abiotic Processes on Marine Snow in the Upper Ocean

The observations presented here show that physical dynamics in the mixed layer can play a key role in particle transformations and sinking carbon export from the upper ocean. Turbulence is required to produce and maintain a pool of marine snow aggregates that sink to depth, yet too much turbulence fragments them, thereby decreasing their sinking velocities and export potential. The largest particles, as measured by the maximum particle size metric, D_{cdf}, were found for a KE_{diss} of roughly 10^{-7} W kg^{-1} (Fig. 4b), suggesting that the KE_{diss} threshold between aggregation and disaggregation should be somewhat larger. For MOUS aggregates, shear coagulation and disaggregation rate estimates were balanced at a KE_{diss} value of $3x10^{-7}$ W kg^{-1} (Fig. 5c). Both estimates are somewhat lower than the threshold turbulence levels found by Takeuchi et al. (2019) for the transition from aggregation to disaggregation (~10^{-6} W kg^{-1}). This small discrepancy could easily be due to differences in the particle structure (size distribution, stickiness, morphology, etc.) as well as methodological differences between the two studies.

Upper layer turbulence played an important role in determining the contribution of marine snow aggregates to sinking particle fluxes. The succession of intense storms deepened the mixed layer, which rapidly shoaled after each storm passed, leading to the isolation of large aggregates just beneath the mixed layer, similar to the mixed layer pump (Gardner et al. 1995; Dall'Olmo et al. 2016). There, these particles were protected from the intense turbulent shear levels near the sea surface and the lower turbulence levels enabled increases in their sizes through coagulation and, in turn, higher sinking rates. The rapid succession of storms repeated this process, creating even larger marine snow aggregates that finally sank to depth (Fig. 8).

The sequence of intense storms both created and destroyed marine snow particles within the upper layer of water column (Figs. 4, 5 & 8). As shown in Fig. 5a, upper layer total particle volumes increased and decreased by factors greater than two in just a few days in response to the intense storms and the pauses between them. Contrasting this trend, turnover time scales for POC stocks in the upper ocean were weeks to months. Turnover time scales for the production of POC ($\int$POC/NPP) were about a week or two, while turnover time estimates for POC export were months (Table 1). This result implies that marine snow particles were being rapidly created and destroyed, yet nearly all of the particle mass, as measured by the POC concentration, was retained in the upper ocean. This successive reworking of particles due to the repeated passages of intense storms led to a decoupling between aggregate volume, particle mass, primary production and sinking particle fluxes.

This successive reworking of aggregates will also likely reduce the efficiency of the biological pump by increasing the residence times of POC in the upper ocean, enabling more time for microbes and metazoans to colonize, remineralize and graze these particles (Iversen and Ploug, 2013; Collins et al. 2015). The nature of this recycling of particulate materials will present a challenge for observing and modeling the mechanisms regulating important carbon cycling metrics, such as e-ratios and remineralization length scales. It also suggests that assessments and parameterizations of the physical aggregation and disaggregation of marine snow need to be included in observational and numerical studies of the biological carbon pump.

4.2 Impacts of Biotic Processes on Marine Snow Dynamics in the Mesopelagic

The two size-class model of the fates of aggregates in the mesopelagic zone provides many insights into marine snow dynamics. First, we show that biotic processes in the mesopelagic zone were disaggregating marine snow into smaller particles (< 0.5 mm). This transformation is likely related to the interaction of large sinking particles with zooplankton, as their appearance corresponded to an increase in zooplankton abundance and marine snow-zooplankton interaction rates (Fig. 7de), and there are no other hypothesized sources for smaller particles emerging within the ECWs. The roughly 1% per day estimated rate corresponded to nearly a 30% increase in small particle abundance for the 25-day study, accounting for much (but not all) of the observed increases shown in Fig. 7ab. These results strongly suggest that zooplankton-particle interactions, via consumption, sloppy feeding, fragmentation by swimming action, or a combination thereof, were the likely source (e.g., Dilling et al. 1998; Dilling and Alldredge, 2000; Goldthwait et al. 2004; Steinberg and Landry, 2017). Further, the biological transformation of smaller particles from marine snow provides a mechanism for the delivery of small particles (D ≤ 0.5 mm) into the mesopelagic zone independent of the sinking of small particles directly from the sea surface (Richardson and Jackson, 2007).

The two size-class model also provides retrievals of the particle consumption rate (γ) of 0.12 d^{-1} (for both w_L models; Table 2). This value is considerably higher than microbial O_2 consumption rates that were made on individual particles at this site (< 0.03 d^{-1}; Belcher et al. 2016). In situ particle respiration rate determinations made during the EXPORTS-NA study were also much smaller than the retrieved values of γ, ranging from 0.02 to 0.06 d^{-1} for all observations below ~100 m (Nicola Paul, pers. comm., 2025). This difference in rates supports the likely dominant role of zooplankton consumption of sinking aggregates in the mesopelagic zone compared to particle associated microbial decomposition. This finding is also similar to conclusions from a recent meta-analysis of particle associated O_2 consumption rates and sinking POC remineralization rates estimated from sinking POC flux profiles (Bressac et al. 2024).

Together these findings support recent studies suggesting that biologically-mediated processes are a critical component of flux attenuation with depth (Giering et al. 2014; 2023; Collins et al. 2015; Briggs et al. 2020) and yet are poorly represented processes in models of the biological pump (Henson et al. 2022; Burd, 2024). Thus, both abiotic and biotic particle aggregation and disaggregation processes need to be included in observational assessments and numerical models of the biological pump.

4.3 Impacts of the Temporal Changes in Marine Snow Characteristics

The nature of the marine snow aggregates changed over the course of the EXPORTS-NA study, becoming more abundant, larger, fluffy and more porous (Figs. 2 & 4d). However, it is unclear whether these changes impacted their sinking speed. Evidence for temporal changes in the sinking speed of marine snow particles during EXPORTS-NA was found by Romanelli et al. (2024). They compared paired marine snow catcher collections and sediment trap deployments and found that the sinking velocity for fast-sinking particles above 200 m increased from roughly 17 m d^{-1} to nearly 100 m d^{-1} over the course of the study (see Figure 3 in Romanelli et al. 2024). “Fast sinking particles” in that study included both small, fast-sinking particles and fast-sinking aggregates collected from the tray on the bottom of the MSC.

In order to evaluate Romanelli et al. (2024)'s finding that aggregate sinking speeds increased over the course of the EXPORTS-NA study, the two size-class model was reconfigured, replacing the constant-in-time marine snow sinking rate, w_L, with a sinking speed that was a linear function of day of sampling. Model coefficients were determined as before (Supplementary Section S11) and ensemble mean retrievals and uncertainties are given in Table 2. We find using the time-dependent w_L model that the marine snow sinking speeds increased by ~1.2 m d^{-1} each day over the course of the study, while the values of the other model coefficients were largely unaltered from the constant in time w_L case. This increase in sinking speed corresponded to $w_L(t)$ changing from 52 m d^{-1} on May 4 to 82 m d^{-1} by May 29, an increase of 30 m d^{-1}. We speculate that these increases were due to the increase in the sizes of sinking aggregates (see also Romanelli et al. 2024), although resolution of this issue is beyond the scope of this contribution. This result supports the findings in Romanelli et al. (2024) of increased sinking speeds for fast sinking aggregates and points to important changes in the characteristics of marine snow particles during the EXPORTS-NA study.

The nature of the observed changes in particle characteristics over time may be related to the processes of sequential building and destroying of aggregates in the mixed layer, driven by the repeated passings of intense storms. We postulate that this successive reworking of particles caused an increase in their porosity during the study. Turbulence limits the size of marine snow aggregates by shearing them into two or more fragments by the smallest eddies in the flow, the Kolmogorov scale (Alldredge et al. 1990; Takeuchi et al. 2019). Laboratory experiments on marine aggregates show that individual shear disaggregation events result in pairs of fragmented particles most of the time (Alldredge et al. 1990; Song et al. 2024). These large fragments should have a similar fractal nature to their parent, and when coagulated again, the resulting aggregates should become more fractal and hence, more porous. This hypothesis, which should hold for the case of the successive reworking of the same particulate material, is consistent with observations of particle porosity growing over time (Fig. 3c) and the emergence of MOUSs (Fig. 3a & S5). The net result of these competing processes will vary as a function of the coupling among food web, particle, and physical oceanographic dynamics (Fig. 8), presenting a challenge for observing and modeling the mechanisms regulating important carbon cycling metrics, such as e-ratios and remineralization length scales.

4.4 The Importance of Lagrangian Sampling

The present analysis of marine snow dynamics was advantaged by the Lagrangian sampling design employed during the EXPORTS-NA study (Erickson et al. 2023; Johnson et al. 2024). The fact that sinking particles could actually be tracked in time gave confidence in the assessments of marine snow dynamics made here. The EXPORTS-NA study leveraged the retentive nature of an anticyclonic eddy to allow observations of coupled ecological / biogeochemical processes to be made in as close to a Lagrangian fashion as possible. Johnson et al. (2024) demonstrated, through an analysis of physical oceanographic data, that core eddy waters below ~100 m were retained within the eddy throughout the study. The UVP observations inside and outside of the eddy core waters supported this analysis, showing that the increase in large aggregates within the eddy core waters came from their sinking from the euphotic zone above the eddy interior, compared with the UVP profiles outside of the eddy center (Figs. 2a & b). The quasi-Lagrangian sampling scheme essentially eliminated lateral transport processes for the eddy core waters that would have acted to obscure the signals associated with the fates of the sinking marine snow that were the aim of this study. Thus, our focused sampling in an anticyclonic eddy provided a near-pristine laboratory in which to understand the relationships among particle dynamics and sinking particles fluxes. In all, this work illustrates the importance of Lagrangian sampling designs to provide the required observational data for understanding the biological pump, particularly for sites with high eddy kinetic energy levels (Briggs et al. 2011; Johnson et al. 2024).

It should also be mentioned that, although the eddy core waters were retained throughout the study, substantial exchanges of surface water masses above the eddy core were observed due to enhanced Ekman transport as each storm passed the site (Johnson et al. 2024). During the four storm events, anywhere from 20 to 75% of the surface water parcels above the eddy's core were exchanged with waters from outside. This observation raises two important points. The first is that the interpretations of temporal changes in surface water properties in this data set across the periods when the storms occurred should be made with caution. The second is that it seems likely that the sampling scheme for the EXPORTS-NA study would have successfully linked the formation of particles in the mixed layer to their transport through the mesopelagic if the storm forcings were not anomalously intense (see Fig. 16 in Johnson et al. 2024).

4.5 Closing Thoughts

The importance of both biotic and abiotic processing of sinking marine snow aggregates demonstrated here suggest that inclusion of these processes should lead to reductions in uncertainties in Earth system model predictions. Recently, Henson et al. (2024) published a compilation of expert assessments on needed improvements in the state of knowledge of processes required to reduce uncertainties in Earth System Model predictions. Their focus was on three major predictive challenges, biological contributions to changes in alkalinity, net primary production and interior respiration, and summarized the expert assessments of the importance and present level of uncertainty of a multitude of contributing processes for each challenge. Their study suggests that to reduce uncertainties in Earth system model predictions of interior respiration processes, a high level of importance should be placed on improvements for assessing biotic fragmentation, aggregation and particle characteristics (e.g. size, porosity, etc.), all consistent with the present findings (see Table 3 in Henson et al. [2024]). However, their summary of expert opinions suggests that zooplankton consumption and abiotic fragmentation processes should have lower levels of importance, contrary to the present findings.

Our results point to the importance of the coupling among the processes of abiotic and biotic fragmentation, particle aggregation (both biotic and abiotic) and biotic consumption (by both microbes and metazoans) on the characteristics and dynamics of marine snow and its response to changing environmental conditions. In essence, we show that abiotic processes in the surface waters are in fact prepping sinking aggregates before they sink into the ocean interior and run the biological gauntlet of grazers and consumers. The interactions among these processes have not been considered in Earth system models and the present observations suggest that somehow, they should be included. Although it is well recognized that there are costs to any additions to a numerical model's complexity (Martin et al. 2024), quantitative assessments of their importance in an Earth system modeling setting are essential. It is clear that there are large uncertainties in present assessments of carbon cycling and storage due to the ocean's biological pump for the contemporary ocean and its future state (Wilson et al. 2022; Doney et al. 2024). Reductions in these uncertainty levels can only be obtained through improving our predictive understanding of the underlying processes. It is hoped that through the coupled observations, analysis and modeling can we achieve these goals.

References:

Alldredge, A.L., Granata, T.C., Gotschalk, C.C., Dickey, T.D. (1990). The physical strength of marine snow and its implications for particle disaggregation in the ocean. *Limnol. Oceanogr.*, ***35***, 1415-1428, https://doi.org/10.4319/lo.1990.35.7.1415.

Alldredge, A.L., & Gotschalk, C. (1988). In situ settling behavior of marine snow. *Limnol. Oceanogr.*, **33**, 339–351, https://doi.org/10.4319/lo.1988.33.3.0339.

Alldredge, A.L. & Silver, M.W., (1988). Characteristics, dynamics and significance of marine snow. *Prog. Oceanogr.*, **20**, 41-82, https://doi.org/10.1016/0079-6611(88)90053-5.

Belcher, A., Iversen, M., Giering, S., Riou, V., Henson, S.A., Berline, et al. (2016). Depth-resolved particle-associated microbial respiration in the northeast Atlantic, *Biogeosciences*, **13**, 4927–4943, https://doi.org/10.5194/bg-13-4927-2016.

Bressac, M., Laurenceau-Cornec, E.C., Kennedy, F., Santoro, A.E., Paul, N.L., Briggs, N., et al. (2024). Decoding drivers of carbon flux attenuation in the oceanic biological pump. *Nature* ***633****, 587–593,* https://doi.org/10.1038/s41586-024-07850-x.

Briggs, N., Dall'Olmo, G., and Claustre, H. (2020). Major role of particle fragmentation in regulating biological sequestration of CO_2 by the oceans. *Science*, **367**, 791-793, https://doi.org/10.1126/science.aay1790.

Briggs, N., Perry, M.J., Cetinić, I., Lee, C., D'Asaro, E., Gray, A.M., and Rehm, E. (2011). High-resolution observations of aggregate flux during a sub-polar North Atlantic spring bloom. *Deep-Sea Res. Part I*, **58**, 1031-1039, https://doi.org/10.1016/j.dsr.2011.07.007.

Brzezinski, M. A., Johnson, L., Estapa, M., Clevenger, S., Roca-Martí, M., Romanelli, E., et al. (2024). Physical mechanisms sustaining silica production following the demise of the diatom phase of the North Atlantic spring phytoplankton bloom during EXPORTS. *Global Biogeochem. Cycles*, **38**, e2023GB008048, https://doi.org/10.1029/2023GB008048.

Buesseler, K. O. & Boyd, P.W., (2009). Shedding light on processes that control particle export and flux attenuation in the twilight zone of the open ocean. *Limnol. Oceanogr.* **54**, 1210–1232, https://doi.org/10.4319/lo.2009.54.4.1210.

Buesseler, K.O., Boyd, P.W., Black, E.E., Siegel, D.A. (2020). Metrics that matter for assessing the ocean biological carbon pump. *Proc. Natl. Acad. Sci. U.S.A.*, **117**, 9679-9687, https://doi.org/10.1073/pnas.1918114117.

Burd, A.B., Modeling the Vertical Flux of Organic Carbon in the Global Ocean. (2024). *Ann. Rev. Mar. Sci.*, **16**, https://doi.org/10.1146/annurev-marine-022123-102516,

Burd, A.B., and G.A. Jackson. (1997). Predicting particle coagulation and sedimentation rates for a pulsed input. *J. Geophys. Res.* **102**(C5), 10,545–10,561, https://doi.org/10.1029/96JC03592,

Burd, A.B., and G.A. Jackson, Particle aggregation. (2009). *Ann. Rev. Mar. Sci.*, **1**, 65-90, https://doi.org/10.1146/annurev.marine.010908.163904.

Burd, A.B., Hansell, D.A., Steinberg, D.K., Anderson, T.R., Arístegui, J., Baltar, F., et al., (2010). Assessing the apparent imbalance between geochemical and biochemical indicators of meso-and bathypelagic biological activity: what the@ $♯! is wrong with present calculations of carbon budgets?. *Deep Sea Res., II*, **57**, 1557-1571, https://doi.org/10.1016/j.dsr2.2010.02.022.

Cael, B.B., E.L. Cavan, and G.L. Britten, (2021). Reconciling the size-dependence of marine particle sinking speed. *Geophys. Res. Lett.*, **48**(5), https://doi.org/10.1029/2020GL091771.

Clevenger S.J., C.R. Benitez-Nelson, M. Roca-Martí, W. Bam, M. Estapa, J.A. Kenyon, et al., (2024), Carbon and silica fluxes during a declining North Atlantic spring bloom as part of the EXPORTS program. Marine Chemistry **258**, 104346. https://doi.org/10.1016/j.marchem.2023.104346.

Collins, J.R., B.R. Edwards, K. Thamatrakoln, J.E. Ossolinski, G.R. DiTullio, K.D. Bidle, et al. (2015). The multiple fates of sinking particles in the North Atlantic Ocean. *Global Biogeochemical Cycles*, **29**, 1471-1494, https://doi.org/10.1002/2014GB005037.

Cram, J. A., T. Weber, S.W. Leung, A.M.P. McDonnell, J.-H. Liang, and C. Deutsch, (2018). The role of particle size, ballast, temperature, and oxygen in the sinking flux to the deep sea. *Global Biogeochemical Cycles*, 32, 858–876. https://doi.org/10.1029/2017GB005710.

Dall'Olmo, G., J. Dingle, L. Polimene, R.J. Brewin, H. Claustre, (2016). Substantial energy input to the mesopelagic ecosystem from the seasonal mixed-layer pump. *Nature Geoscience*, **9**, 820-823, https://doi.org/10.1038/ngeo2818.

Dilling, L., & A.L. Alldredge, (2000). Fragmentation of marine snow by swimming macrozooplankton: a new process impacting carbon cycling in the sea*. Deep-Sea Res. I*, **47**, 1227–1245, https://doi.org/10.1016/S0967-0637(99)00105-3.

Dilling, L., J. Wilson, D. Steinberg, A. Alldredge, (1998). Feeding by the euphausiid, *Euphausia pacifica*, and the copepod, *Calanus Pacificus*, on marine snow. *Mar. Ecol. Prog. Ser.*, **170**, 189-20, https://doi.org/10.3354/meps170189.

Doney, S. C., Mitchell, K. A., Henson, S. A., Cavan, E., DeVries, T., Gruber, N., et al., (2024). Observational and numerical modeling constraints on the global ocean biological carbon pump. *Global Biogeochem. Cycles*, **38**, https://doi.org/10.1029/2024GB008156.

Doney S.C., Wolfe W.H., McKee D.C. and Fuhrman J.G., (2025). The science, engineering, and validation of marine carbon dioxide removal and storage. *Ann. Rev. Mar. Sci.*, **17**, 55-81, https://doi.org/10.1146/annurev-marine-040523-014702.

Drago, L., (2023). Analyse globale de la pompe à carbone biologique à partir de données en imagerie quantitative. Biodiversité et Ecologie. Sorbonne Université, 2023. Français. ⟨NNT : 2023SORUS562⟩. ⟨tel-04483392⟩.

Ducklow, H.W., D.K. Steinberg, K.O. Buesseler, (2001). Upper ocean carbon export and the biological pump. *Oceanography*, **14**, 50-58.

Durkin C.A., K.O. Buesseler, I. Cetinić, M.L. Estapa, R.P. Kelly, M. Omand, (2021). A visual tour of carbon export by sinking particles. *Global Biogeochem. Cycles,* **35**, e2021GB006985. https://doi.org/10.1029/2021GB006985.

Erickson, Z.K., E. Fields, L. Johnson, A.F. Thompson, L.A. Dove, E. D'Asaro, D.A. Siegel, (2023). Eddy tracking from in situ and satellite observations. *J. Geophys. Res.*, **128**, e2023JC019701. https://doi.org/10.1029/2023JC019701.

Franks, P.J.S., Inman, B.G., MacKinnon, J.A., Alford, M.H. and Waterhouse, A.F. (2022). Oceanic turbulence from a planktonic perspective. *Limnol. Oceanogr.*, **67**, 348-363. https://doi.org/10.1002/lno.11996.

Gardner, W.D., S.P. Chung, M.J. Richardson, & I.D. Walsh, (1995). The oceanic mixed-layer pump. *Deep Sea Res. Part II*, **42**, 757-775, https://doi.org/10.1016/0967-0645(95)00037-Q.

Giering, S. L. C., R. Sanders, A.P. Martin, S.A. Henson, J.S. Riley, C.M. Marsay, D.G. Johns, (2017). Particle flux in the oceans: Challenging the steady state assumption, *Global Biogeochem. Cycles*, **31**, 159–171, https://doi.org/10.1002/ 2016GB005424.

Giering, S.L., R. Sanders, R.S. Lampitt, T.R. Anderson, C. Tamburini, M. Boutrif, et al., (2014). Reconciliation of the carbon budget in the ocean's twilight zone. *Nature*, **507**, 480-483, https://doi.org/10.1038/nature13123.

Giering, S.L.C., R. Sanders, S. Blackbird, N. Briggs, F. Carvalho, H. East, et al., (2023). Vertical imbalance in organic carbon budgets is indicative of a missing vertical transfer during a phytoplankton bloom near South Georgia (COMICS). *Deep Sea Res. Part II*, **209**, 105277, https://doi.org/10.1016/j.dsr2.2023.105277.

Goldthwait, S., J. Yen, J. Brown, A. Alldredge, (2004). Quantification of marine snow fragmentation by swimming euphausiids, *Limnol. Oceanogr.*, **49**, 940-952, https://doi.org/10.4319/lo.2004.49.4.0940.

Hartman, S.E., Bett, B.J., Durden, J.M., Henson, S.A., Iversen, M., Jeffreys, R.M., et al. (2021). Enduring science: three decades of observing the Northeast Atlantic from the Porcupine Abyssal Plain Sustained Observatory (PAP-SO). *Prog.Oceanogr.*, **191**, https://doi.org/10.1016/j.pocean.2020.102508.

Henson, S. A., A. Yool, and R. Sanders (2015), Variability in efficiency of particulate organic carbon export: A model study, *Global Biogeochem. Cycles*, **29**, 33–45, https://doi.org/10.1002/2014GB004965.

Henson, S.A., Laufkötter, C., Leung, S. *et al.* (2022), Uncertain response of ocean biological carbon export in a changing world. *Nat. Geosci.* **15**, 248–254, https://doi.org/10.1038/s41561-022-00927-0.

Henson, S., C.A. Baker, P. Halloran, A. McQuatters-Gollop, S. Painter, et al., (2024). Knowledge gaps in quantifying the climate change response of biological storage of carbon in the ocean. *Earth's Future*, **12**, e2023EF004375, https://doi.org/10.1029/2023EF004375.

Iversen, M.H., (2023). Carbon Export in the Ocean: A Biologist's Perspective. *Ann. Rev. Mar. Sci.*, **15**, 357-381, https://doi.org/10.1146/annurev-marine-032122-035153.

Iversen, M.H. & Ploug, H., (2013). Temperature effects on carbon-specific respiration rate and sinking velocity of diatom aggregates–potential implications for deep ocean export processes. *Biogeosciences*, *10*(6), 4073-4085, https://doi.org/10.5194/bg-10-4073-2013.

Jackson G.A., (1990). A model of the formation of marine algal flocs by physical coagulation processes. *Deep-Sea Res. A,* **37**, 1197–211, https://doi.org/10.1016/0198-0149(90)90038-W.

Johnson, L., D.A. Siegel, A.F. Thompson, E. Fields, Z.K. Erickson, I. Cetinić, I., et al., (2024). Assessment of oceanographic conditions during the North Atlantic EXport processes in the ocean from RemoTe Sensing (EXPORTS) Field campaign. *Prog. Oceanog.*, 103170, https://doi.org/10.1016/j.pocean.2023.103170.

Kriest, I., (2002). Different parameterizations of marine snow in a 1D-model and their influence on representation of marine snow, nitrogen budget and sedimentation. *Deep Sea Res. Part I*, **49**, 2133-2162, https://doi.org/10.1016/S0967-0637(02)00127-9.

Lacour, L., Llort, J., Briggs, N., Strutton, P.G. and Boyd, P.W., (2023). Seasonality of downward carbon export in the Pacific Southern Ocean revealed by multi-year robotic observations. *Nature Comm.*, **14**, 1278, https://doi.org/10.1038/s41467-023-36954-7.

Laurenceau-Cornec, E.C., T.E. Trull, D.M. Davies, L. Christina, S. Blain, (2015). Phytoplankton morphology controls on marine snow sinking velocity. *Mar. Ecol. Prog. Ser.*, **520**, 35-56, https://doi.org/10.3354/meps11116**.**

Laurenceau-Cornec, E.C., Le Moigne, F.A., Gallinari, M., Moriceau, B., Toullec, J., Iversen, M.H. , (2019). New guidelines for the application of Stokes' models to the sinking velocity of marine aggregates. *Limnol. Oceanogr.*, **65**(6), 1264-1285. https://doi.org/10.1002/lno.11388.

Le Moigne, F.A., (2019). Pathways of organic carbon downward transport by the oceanic biological carbon pump. *Front. Mar. Sci.*, **6**, 634, https://doi.org/10.3389/fmars.2019.00634.

Logan, B.E., & A.L. Alldredge, (1989). The increased potential for nutrient uptake by flocculating diatoms. *Mar. Biol.*, **101**, 443–450, https://doi.org/10.1007/BF00541645.

Marañón, E., (2015). Cell size as a key determinant of phytoplankton metabolism and community structure. *Ann. Rev. Mar. Sci.*, **7**(1), 241-264, https://doi.org/10.1146/annurev-marine-010814-015955.

Martin, A.P., Dominguez, A.B., Baker, C.A., Baumas, C.M., Bisson, K.M., Cavan, E., Freilich, M., Galbraith, E., Galí, M., Henson, S. and Kvale, K.F., (2024). When to add a new process to a model–and when not: A marine biogeochemical perspective. *Ecological Modelling*, **498**, 110870, https://doi.org/10.1016/j.ecolmodel.2024.110870.

McDonnell, A. M., & Buesseler, K. O. (2010). Variability in the average sinking velocity of marine particles. *Limnology and Oceanography*, **55**(5), 2085-2096. https://doi.org/10.4319/lo.2010.55.5.2085.

Meyer, M. G., Brzezinski, M. A., Cohn, M. R., Kramer, S. J., Paul, N., Sharpe, G., et al. (2024). Size-fractionated primary production dynamics during the decline phase of the

North Atlantic spring bloom. *Global Biogeochem. Cycles*, **38**, e2023GB008019. https://doi.org/10.1029/2023GB008019.

Møller, E.F., P. Thor, T.G. Nielsen, (2003). Production of DOC by *Calanus finmarchicus*, *C. glacialis* and *C. hyperboreus* through sloppy feeding and leakage from fecal pellets. *Mar. Ecol. Prog. Ser.*, **262**, 185–191, https://doi.org/10.3354/meps262185**.**

Nowicki, M., T. DeVries & D.A. Siegel, (2024). The influence of air-sea CO_2 disequilibrium on carbon sequestration by the ocean's biological pump. *Global Biogeochem. Cycles*, **38**, e2023GB007880. https://doi.org/10.1029/2023GB007880.

Picheral, M., L. Guidi, L. Stemmann, D.M. Karl, G. Iddaoud, G. Gorsky, (2010). The Underwater Vision Profiler 5: An advanced instrument for high spatial resolution studies of particle size spectra and zooplankton. *Limnol. Oceanogr.: Methods*, **8**, 462-473, https://doi.org/10.4319/lom.2010.8.462.

Richardson T.L., G.A. Jackson, Small phytoplankton and carbon export from the surface ocean. *Science*, 315, 838-840, https://doi.org/10.1126/science.1133471. (2007).

Romanelli, E., Giering, S.L.C., Estapa, M., Siegel, D.A. and Passow, U. (2024), Can intense storms affect sinking particle dynamics after the North Atlantic spring bloom? *Limnol. Oceanogr.*, **69**(12), 2963-2974, https://doi.org/10.1002/lno.12723.

Siegel, D. A., Buesseler, K. O., Behrenfeld, M. J., Benitez-Nelson, C. R., Boss, E., Brzezinski, M. A., et al., (2016). Prediction of the export and fate of global ocean net primary production: The EXPORTS science plan. *Frontiers in Marine Science*, **3**, https://doi.org/10.3389/fmars.2016.00022.

Siegel, D.A., Cetinić, I., Graff, J.R., Lee, C.M., Nelson, N., Perry, M.J., Ramos, I.S., Steinberg, D.K., Buesseler, K., Hamme, R. and Fassbender, A.J., (2021). An operational overview of the EXport Processes in the Ocean from RemoTe Sensing (EXPORTS) Northeast Pacific field deployment. *Elem. Sci. Anth.*, **9**(1), p.00107, https://doi.org/10.1525/elementa.2020.00107.

Siegel, D.A., T. DeVries, I. Cetinić, K.M. Bisson, (2023a). Quantifying the Ocean's Biological Pump and its Carbon Cycle Impacts on Global Scales. *Ann. Rev. Mar. Sci.*, **15**, 329-356, https://doi.org/10.1146/annurev-marine-040722-115226.

Siegel, D.A., I. Cetinić, A.F. Thompson, N.B. Nelson, M. Sten, M. Omand, et al., (2023b). EXport Processes in the Ocean from RemoTe Sensing (EXPORTS) North Atlantic sensor calibration and intercalibration documents. https://doi.org/10.1575/1912/66998.

Sieracki, M.E., P.G. Verity, D.K. Stoecker, (1993). Plankton community response to sequential silicate and nitrate depletion during the 1989 North Atlantic spring bloom. *Deep Sea Res. Part* II, **40**, 213-225, https://doi.org/10.1016/0967-0645(93)90014-E.

San Soucie, J. E., Girdhar, Y., Johnson, L., Peacock, E. E., Shalapyonok, A., & Sosik, H. M. (2024). Spatiotemporal topic modeling reveals storm-driven advection and stirring control plankton community variability in an open ocean eddy. *J. Geophys. Res. Oceans,* **129**, e2024JC020907, https://doi.org/10.1029/2024JC020907.

Song Y., A.B. Burd, M.J. Rau, (2023). The deformation of marine snow enables its disaggregation in simulated oceanic shear. *Front. Mar. Sci*. **10**:1224518, https://doi.org/10.3389/fmars.2023.1224518.

Steinberg, D. K., J. S. Cope, S. E. Wlson, and T. Kobari (2008). A comparison of mesopelagic mesozooplankton community structure in the subtropical and subarctic North Pacific Ocean. *Deep-Sea Res. II*, **55**, 1615-1635, https://doi.org/10.1016/j.dsr2.2008.04.025.

Steinberg, D.K., Van Mooy, B.A., Buesseler, K.O., Boyd, P.W., Kobari, T. and Karl, D.M., 2008. Bacterial vs. zooplankton control of sinking particle flux in the ocean's twilight zone. *Limnology and Oceanography*, **53**, 1327-1338, https://doi.org/10.4319/lo.2008.53.4.1327.

Steinberg, D. K., Stamieszkin, K., Maas, A. E., Durkin, C. A., Passow, U., Estapa, M. L., et al., The outsized role of salps in carbon export in the subarctic Northeast Pacific Ocean. *Global Biogeochem. Cycles*, **37**, e2022GB007523. https://doi.org/10.1029/2022GB007523, (2023).

Steinberg, D.K., M.R. Landry, (2017). Zooplankton and the ocean carbon cycle. *Ann. Rev. Mar. Sci.*, **9**, 413-444, https://doi.org/10.1146/annurev-marine-010814-015924.

Stemmann, L., Jackson, G.A. and Ianson, D., (2004). A vertical model of particle size distributions and fluxes in the midwater column that includes biological and physical processes—Part I: model formulation. *Deep Sea Res. Part I:* **51**, 865-884, https://doi.org/10.1016/j.dsr.2004.03.001.

Stephens, B.M., Durkin, C.A., Sharpe, G., Nguyen, T.T., Albers, J., Estapa, M.L., Steinberg, D.K., Levine, N.M., Gifford, S.M., Carlson, C.A. and Boyd, P.W., (2024). Direct observations of microbial community succession on sinking marine particles, *The ISME Journal*, **18**, wrad010, https://doi.org/10.1093/ismejo/wrad010.

Takeuchi, M., Doubell, M.J., Jackson, G.A. *et al.,* (2019). Turbulence mediates marine aggregate formation and destruction in the upper ocean. *Sci Rep*, **9**, 16280, https://doi.org/10.1038/s41598-019-52470-5.

Uitz, J., H. Claustre, A. Morel, S.B. Hooker, (2006). Vertical distribution of phytoplankton communities in open ocean: An assessment based on surface chlorophyll. *J. Geophys. Res.*, **111**(C08005), 1–23, https://doi.org/10.1029/2005JC003207.

Wilson, J. D., Andrews, O., Katavouta, A., de Melo Viríssimo, F., Death, R. M., Adloff, M., et al. (2022). The biological carbon pump in CMIP6 models: 21st century trends and uncertainties. *Proc. Nat. Acad. Sci. USA*, **119**, e2204369119. https://doi.org/10.1073/pnas.2204369119.

Acknowledgements:

The authors would like to acknowledge support from the NASA Ocean Biology and Biogeochemistry program, the National Science Foundation Biological and Chemical Oceanography programs and the Woods Hole Oceanographic Institution's Ocean Twilight Zone study. We greatly acknowledge the cooperation, skill and commitment of the Captains, Crews, Research Technicians and Shore-Based Staffs of the RRS James

Cook (JC214), RRS Discovery (DY130 & DY131) and the R/V Sarmiento de Gamboa (SG2105) for making the EXPORTS-NA field deployment a reality. Special thanks to Laura Lorenzoni (NASA HQ), Mike Sieracki (formally NSF BIO-OCE), Paula Bontempi (formally NASA HQ), and Quincy Allison and his team (ESPO - NASA AMES) for their vision, support and energy throughout the development and implementation of the EXPORTS field campaign. Last, we like to thank our many EXPORTS colleagues for their brilliance, energy, dedication, hard work, support, collegiality and patience.

Data Availability:

All EXPORTS data used here is archived at NASA's SeaWiFS Bio-optical Archive and Storage System (SeaBASS) under the EXPORTS Experiment (https://seabass.gsfc.nasa.gov/experiment/EXPORTS). Data collected during the EXPORTSNA field expedition onboard the Sarmiento the Gamboa was archived under the OTZ_WHOI experiment (10.5067/SeaBASS/OTZ_WHOI/DATA001) and cruise name SG2105. The intercalibrated UVP particle size distribution data set presented here is available at https://doi.org/10.31223/X58709. To find out information about all the data collected during the EXPORTS field campaigns, their data repositories and availability, please visit: https://sites.google.com/view/oceanexports/home.

Supplementary Materials:

S1 - Characterizing Marine Snow Aggregates

Marine particles can be characterized in many ways, such as using their size distribution, sinking speed, excess density, porosity, biogeochemical content, opacity, morphology, and source materials (McDonnell et al. 2015; Lombard et al. 2019; Iversen, 2023). The focus of this paper is on those particles that contribute to sinking particulate organic carbon (POC) fluxes using in situ determinations of the particle size spectrum from image analysis from Underwater Video Profilers (UVP) observations. Of particular interest are marine snow aggregates, which are defined as aggregates with equivalent spherical diameters greater than 0.5 mm (e.g., Alldredge and Silver, 1988). We will also assess the dynamics of small particles and aggregates ($D < 0.5$ mm) as well as very large marine snow aggregates (MOUSs - Marine snow Of Unusual Size, *in sensu* D.P. Roberts), which we define as aggregates with $D > 5$ mm.

S2 - Characterizing Marine Aggregates Using In Situ Imagery

The abundance and size of large particles and aggregates were quantified as a function of depth using Underwater Vision Profiler 5 (UVP; Picheral et al. 2010). The UVP illuminates approximately 1 L of seawater imaged at a pixel resolution of ~50 μm. Particles are identified as contiguous pixels whose area is converted to equivalent spherical diameters (D_{esd}). For simplicity, we will often refer to D_{esd} as D. UVP deployments were made from each of the three ships, profiling from the surface down to at least 500 m. Excluding days with weather interruptions, 6 to 9 UVP profiles were made each day within the ECWs. Particle abundance size distributions are determined for 25 logarithmically distribution bins with center bin diameters ranging from 0.09 to 23.9 mm. In standardizing the UVP data from the three ships, the first two bins were removed from consideration, making 0.13 mm the smallest particle diameter bin center reliably imaged (Siegel et al. 2023b). Here, particle abundance size distributions are averaged into 5 m vertical bins for equivalent spherical diameters ranging from 0.13 to 10 mm. Given the UVP's sampling frequency (6 Hz) and typical CTD frame lowering rates, nearly 100 individual scans make up each 5-m vertical average, corresponding roughly to 100 L of seawater. Particle size spectra are reported here as particle volume spectra in differential form (units are ppmV per mm bin width). This representation accentuates changes in the particle size spectra compared to visualizations made with particle abundance spectra and do not require the simultaneous reporting of bin dimensions (Jackson et al. 1997; Zhang et al. 2023). Further details of the UVP processing including the standardizing of observations from the three ships are included in Siegel et al. (2023b).

Total particle abundances and volumes are calculated as the integral of the differential particle number and volume spectra over the measured particle diameters, respectively. The size of the largest particles robustly sampled, D_{cdf}, is quantified as the size of the 95th percentile of the cumulative probability distribution of the daily mean differential particle volume. The 95th percentile threshold was selected via experimentation to reduce noise in the D_{cdf} values to intermittency in the UVP's sampling of the very largest particles. Note that values of D_{cdf} are not the very largest particles observed as 5% of the total particle volume will have particle diameters greater than D_{cdf}.

Aggregate abundances were quantified from an analysis of UVP's vignette images of large individual objects (≥ 1 mm). This classification was conducted first by using MorphoCluster (Schröder et al. 2020), which enables the fast, human-assisted assimilation of likewise-appearing objects into clusters and subsequent classification. Vignette images and their classification were uploaded to EcoTaxa (https://ecotaxa.obs-vlfr.fr) where classifications were further checked. Abundances of "fluffy" and "very fluffy" aggregates classified in this manner were binned together into 5 m vertical bins and daily averages (Drago, 2023).

S3 - Characterizing Sinking Particle Speeds as a Function of Size

Particle fluxes depend on the concentration of sinking particles and their sinking speeds. Sinking marine particles gravitationally settle through the water column at rates ranging from a couple meters per day to greater than 100 meters per day (e.g., Alldredge and Gotschalk, 1988; Laurenceau-Cornec et al. 2019; Cael et al. 2021; Steinberg et al. 2023). Particle sinking speeds are regulated by particle size, excess density (ballasting), and morphology (Laurenceau-Cornec et al. 2015; 2019; Cael et al. 2021). However, an accurate relationship for sinking speed that incorporates these factors remains elusive. Consequently, particle sinking speeds are often modeled as functions of particle size alone (Burd and Jackson, 1997; Kriest, 2002; Stemmann et al., 2004; Cael et al., 2021; Lacour et al. 2023).

Sinking speed size distributions were estimated from the temporal evolution of UVP determined particle abundance distributions following the methods introduced by Lacour et al. (2023). For each size bin, particle abundance time-depth distributions were first smoothed using a LOESS fit (Fig. S4). Six to ten particle abundance isosurfaces were selected and the slope of the depth-time relationships were calculated. Only observations from the period May 14 to 25 and below 100 m and bin centers from 0.13 to 3.65 mm were used. The mean and standard deviation of ensemble of isosurface depth vs. time slopes were then calculated and reported in Figure 2c.

S4 - Assessments of Aggregate Abundances from Marine Snow Catcher Collections:

Sinking aggregates (*D* >0.1 mm) were collected below the mixed layer down to depths of 500 m using four Marine Snow Catchers (MSC) as detailed by Romanelli et al. (2024). After retrieval, each MSC was placed on deck in an upright position for exactly 2 hours to allow the sinking of marine snow aggregates inside a circular plastic tray placed inside the base section of the MSC. Right after, the water collected in the base overlying the tray was gently sampled and the tray was transferred to the lab to manually pick individual aggregates. The aggregates were sized and counted under a dissecting scope.

S5 - Assessments of Solid Fractions of Sinking and Suspended Particles:

Particle solid fractions (= 1 - Porosity) were estimated as the ratio of solid particle component volumes to total particle volume using sediment trap samples and from near-simultaneous large volume pump collections and UVP deployments.

Sinking particle solid fractions were estimated using surface-tethered and neutrally-buoyant arrays of sediment traps with cylindrical trap tubes (0.0113 m^2) carrying either poisoned brine (for bulk measurements of sinking POC, PIC, bSi, and mass flux; Estapa et al. 2021; 2024) or polyacrylamide gel collectors (for particle enumeration, size, and classification; Durkin et al., 2021). POC flux was determined following Estapa et al. (2024). PIC flux was measured by coulometric analysis (Honjo et al., 2000) on gravimetric splits of the same filters used for POC. Biogenic silica was measured by hot alkaline extraction of sample splits filtered onto polycarbonate membranes followed by spectrophotometric analysis (Brzezinski et al., 2024). Polyacrylamide gels were digitally imaged at 7x, 32x, and 115x magnification, then particles were identified and enumerated following methods similar to Durkin et al. (2021). Image pixel size at 32x resolution was intercalibrated with the pixel size at 7x resolution following Jackson et al. (1997). Particle diameter was used to estimate sinking particle volumes, assuming spherical particles. Volume and mass fluxes were finally calculated by normalizing to trap deployment length and collection area. During the third epoch, surface tethered traps were subjected to horizontal velocities exceeding 30 cm s^{-1}. Thus, only data from neutrally-buoyant sediment traps are shown for that deployment. Determinations of solid particle fractions for sinking particles were calculated by first converting the bulk fluxes to mass fluxes of organic matter, opal, and calcium carbonate. Representative component densities were then used to estimate the volume flux of the solid fraction in the particles (POC to organic matter: Lam et al. 2011; bSi to opal: Mortlock and Froelich, 1989; PIC to $CaCO_3$: stoichiometry; densities: Laurenceau-Cornec et al., 2019). These solid fraction volume fluxes were divided by the gel trap determined volume fluxes to estimate solid particle fractions for sinking particles.

For suspended particles, a similar process was used to estimate the solid volume concentration from POC, bSi, and PIC concentrations measured in the > 335 µm size fraction of the large volume pump samples (Clevenger et al. 2024). Particle solid fractions for suspended particles were determined by dividing the solid volume concentrations calculated from the large volume pump samples by total volume concentration of particles larger than 335 µm particles estimated from paired suspended particles UVP profiles.

S6 - Determinations of Turbulent Kinetic Energy Dissipation Rates in the Mixed Layer:

Turbulent kinetic energy dissipation rates (ε or KE_{diss}; W kg^{-1}) were calculated for the upper 50 m of the water column using established similarity scalings described by Lombardo and Gregg (1989) and D'Asaro (2014), or

$$KE_{diss} = 0.58\left(-\frac{g\alpha Q}{\rho_o c_p} + g\beta(E-P)S_o\right) + \frac{1.76(\tau/\rho_o)^{3/2}}{\kappa z} \quad \text{(S1)}$$

The first term represents the contribution from surface buoyancy forcing, where g is gravity, α is the thermal expansion coefficient, Q is the surface net heat flux, ρ_o is a reference density, β is the haline contraction coefficient, *E* is evaporation, *P* is precipitation and S_o is a reference salinity. The second term represents the contribution from momentum input, where τ is the surface wind stress, κ is the von Karmen constant, and *z* is depth from the surface. Surface heat and freshwater fluxes and wind stress were estimated using ship based meteorological measurements processed with the COARE bulk formula. Additional details can be found in Johnson et al. (2024).

S7 - Assessing Particle Biomass from In Situ Particle Imagery

Individual marine snow aggregates are highly porous, which affects both the particle's sinking speed and the relationship between its volume and biomass. Assuming fractal scaling, the mass of an aggregate of size *D*, or *M(D)*, scales as a function of the fractal dimension relative to the size (D_1) and mass (M_1) of the smallest, monomer particle used to construct the aggregate, or

$$\frac{M(D)}{M_1} \propto \left(\frac{D}{D_1}\right)^{F_D} \quad \text{(S2)}$$

For a solid particle, the fractal dimension would be 3, whereas values reported in the literature for marine snow typically range between 1.5 and 2.3 with large uncertainties of its assessment from observational data (Logan and Alldredge 1989; Kilps et al. 1994; Li and Logan 1995; Risović and Martinis 1996; Jackson et al. 1997; Ploug et al. 2008).

The fractal dimension also affects other physical properties of an aggregate, such as how particle mass is projected onto a 2-dimensional image (Giering et al., 2020). The particle size measured from such images (its fractal diameter or equivalent spherical diameter, D_{esd}) will therefore depend on fractal dimension. However, assessments of particle dynamics are correctly calculated using the solid (or conserved) mass of the particle, which is preserved during coagulation and fragmentation. The diameter of the conserved volume (D_C) is the diameter of the sphere obtained by squeezing all the solid material of the particle together and is related to the equivalent spherical diameter by

$$\left(\frac{D_c}{D_1}\right)^3 = A\left(\frac{D_{esd}}{D_1}\right)^{F_D} \qquad \text{(S3)}$$

where the normalization constant is $A = 0.6^{-F_D/2}$ (Stemmann et al., 2004). Methodological details for converting from fractal (f(D_{esd})) to conserved (f(D_c)) representations and back again are presented in below.

The UVP-determined ESD volume distributions were converted to conserved volumes ensuring that total particle numbers remained the same (Jackson, 1990). To achieve this, the size-bin boundaries in the fractal diameter representation are mapped to the conserved diameter representation using Eq. S3. Particles from each D_{esd} sized bin are then distributed to the conserved size-bins. If a D_{esd} sized size bin straddles more than one conserved size-bin, particles are apportioned according to the fraction of the fractal size bin that is within each conserved size-bin. The process is reversed to convert from conserved to fractal representations. This transformation conserves the total number of particles and enables the transformations of marine snow particles to be correctly quantified.

In order to account for the uncertainties in the assumed fractal dimensions in the calculations to follow, an ensemble of calculations is created using a range of particle fractal dimensions from 1.5 to 2.3. The ensemble included both particle fractal dimensions that are constant in time as well as examples that linearly decrease in time to assess the impacts of increasing particle porosity in time. The final ensemble was made up of 21 members. Means and standard deviations of large particle formation rates by coagulation are calculated from the ensemble.

S8 - Quantifying Marine Snow Aggregate Coagulation Rates

Physical processes cause particles to collide with each other, building large particles via the coagulation of smaller ones (Jackson, 1990). The time evolution of the particle size distribution $n(D,t)$ by coagulation can be described by

$$\frac{\partial n(D,t)}{\partial t} = \frac{1}{2}\int_0^D \beta(D-\widetilde{D},\widetilde{D})\,n(D-\widetilde{D},t)\,n(\widetilde{D},t)\,d\widetilde{D} - n(D,t)\int_0^\infty \beta(D,\widetilde{D})\,n(\widetilde{D},t)\,d\widetilde{D} \qquad \text{(S4)}$$

where t is the time, $\beta(D_i,D_j)$ is the coagulation kernel representing the encounter rate of particles of sizes D_i and D_j and the number densities and diameters can either be in projected or conserved forms. The first term on the right-hand side describes the creation of particles of size D by coagulation of smaller particles, while the second term represents the loss of particles of size D by coagulation with other particles. Rectilinear coagulation kernels for fluid shear-driven encounters, $\beta_{sh}(D_i, D_j)$, and differential sedimentation, $\beta_{ds}(D_i, D_j)$, (where a faster sinking particle catches up with a slower sinking one) have the form

$$\beta_{sh}(D_i, D_j) = \frac{1.3}{8}\left(\frac{\varepsilon}{\nu}\right)^{1/2}\left(D_i + D_j\right)^3 \quad \text{(S5a)}$$

$$\beta_{ds}(D_i, D_j) = \frac{\pi}{4}\left(D_i + D_j\right)^2\left|w(D_j) - w(D_i)\right| \quad \text{(S5b)}$$

where ϵ is the turbulent kinetic energy dissipation rate, ν is the water viscosity, and $w(D)$ is the sinking speed of the particle (Burd and Jackson, 2009). An important consequence of the coagulation equation (Eq. S4) is that the formation rate of large particles depends on the particle encounter rate and the product of the particle abundances of appropriate sizes to create particles of size D. In other words, the coagulation rate is a non-linear function of both particle size and particle abundance. Because large particles are less abundant than smaller ones, rates of particle coagulation tend to be greatest for similar-sized particles.

Particle coagulation rates for marine snow particles of unusual size (D > 5 mm) were calculated from depth-averaged particle volume spectra over the 0-50 m layer (Fig. 5b) and the 40-80 m layer (Fig. 6b). These calculations were done using a size-class based discretization of the coagulation equation (Eq. S4) using a turbulent shear coagulation (Eq. S5a), conserved particle abundances and modeled turbulent kinetic energy dissipation rates (Eq. S4) over the ensemble of assumed particle fractal dimensions (see S6). Means and standard deviations of MOUS formation rates by shear coagulation were normalized over the time-series of ensemble of time courses by z-scoring each member of the ensemble, setting the minimum value of each to zero and then averaging over the ensemble.

Formation rates due to differential sedimentation coagulation (Eq. S5b) were also assessed for MOUS aggregates. Conserved particle volume spectra were calculated as detailed above and the mean particle sinking speed spectrum estimated here was used (see Fig. 2c). For the 40 to 80 m layer, where differential settlement should be more important, it was found that rates of shear coagulation were more than twelve times greater than differential sedimentation rates (Fig. S6). Hence, only rates of large particle formation due to shear coagulation are used here.

S9 - Quantifying the Disaggregation of Marine Snow Aggregates

Physical processes can also make smaller particles from larger ones via shear disaggregation (Alldredge et al. 1990; Takeuchi et al. 2019; Song et al. 2024). If the size of a marine snow aggregate is larger than the size of the smallest eddy in the flow, the Kolmogorov scale, turbulence will shear the particle into two or more fragments. Alldredge et al. (1990) found that shear turbulence in tank experiments led to a maximum particle size for marine snow that was a function of the turbulent kinetic energy dissipation rate, or $D_{max} = 0.75\ \varepsilon^{-0.15},$ where the constants are rough averages over multiple experiments. Conserved particle volumes in aggregates larger than D_{max} are redistributed into smaller particles such that 2/3 of the volume goes into the next size class smaller than the maximum particle size and the remaining volume is distributed uniformly among the smaller size classes, following the results of Alldredge et al. (1990).

S10 - Estimating Marine Snow-Zooplankton Encounter Rates

Biotic processes can also work to control the characteristics and size distribution of marine snow. For example, zooplankton consume small particles and can create larger ones in the form of fecal pellets, feeding webs and their carcasses (Stamieszkin et al. 2021; Iversen, 2023; Steinberg et al. 2023). Zooplankton biotic processes also act to transform larger particles back to small ones through sloppy feeding and/or fragmentation by the turbulent shears created by swimming actions (Dilling et al. 1998; Dilling and Alldredge, 2000; Goldthwait et al. 2004). Sloppy feeding can also enhance the solubilization of particles into dissolved forms which are readily available to the mesopelagic microbial community (Møller et al. 2003; Collins et al. 2015).

Key to quantifying the zooplankton mediated particle interactions is the assessment of the zooplankton-particle encounter rate. Here, we derive a simple model for the rate of zooplankton-particle interactions assuming that a population of sinking particles encounters a zooplankter that can detect a sinking particle up to a distance σ away from it. Their interaction rate can be estimated by considering a column of water with cross-sectional area A containing N_Z zooplankton per m^3 and N_P particles per m^3. We assume that the particles sink with a sinking speed of w_p m d^{-1} and as particles sink they encounter the zooplankton. The number of interactions experienced by a single particle in time Δt is

$$n_i = (\pi\sigma^2 w_p \Delta t) N_z \qquad \text{(S6)}$$

where the term in parentheses represents the volume of a cylinder of radius σ swept out in time Δt by a particle sinking with speed w_p. The total number of particles in the volume $\pi\sigma^2 w_p \Delta t$ is equal to $N_p \pi\sigma^2 w_p \Delta t$. Thus, the total number of interactions experienced by all particles is then

$$n_i N_p \pi\sigma^2 \mathrm{w_p} \Delta t = \pi\sigma^2 w_p^2 A \Delta t^2 N_Z N_P \qquad \text{(S7)}$$

and the number of zooplankton-particle interactions per unit volume per unit time is

$$N_i = \pi\sigma^2 w_P N_Z N_P \qquad \text{(S8)}$$

which has units of # interactions m^{-3} d^{-1}.

The parameter σ is an estimate of the average distance over which an individual animal detects a falling particle. Theoretical σ estimates for the estuarine copepod *Acartia tonsa* range from a few tens of microns to almost 100 µm and for open ocean copepods from a few hundred microns to just under 1 mm (Visser, 2001). In the calculations performed here, a value of 1 mm for σ for a constant sinking speed of 50 m d^{-1} are used.

This calculation assumes that the zooplankton and particles are homogeneously distributed over the volume being considered. It also assumes that particles are not removed by zooplankton — i.e., a single sinking particle can interact with multiple zooplankton. However, this should be a minor issue considering the 25 to 100-fold increases in particle-zooplankton interaction rates calculated over the time course of this study (Fig. 7e; Table S1). For example, a sinking particle with a sinking speed of 50 m d^{-1} will take 2 days to sink 100 m. Assuming a particle consumption rate, γ, of 0.1 d^{-1}, sinking particle abundances will decrease over the 100 m interval by about 20% ($\Delta N_P \sim (1-\gamma)^2$). Thus, particle removal will have a relatively minor influence on estimates of zooplankton-particle interactions given the many orders of magnitude changes in interaction rates diagnosed.

Zooplankton abundance (N_Z; individuals m^{-3}) were calculated in 9 discrete depth intervals spanning 0-1000 m from MOCNESS net tows (three day-night pairs on May 11, 17, and 26). At sea samples from each depth interval were split using a Folsom plankton splitter and processed using protocols described in Steinberg et al. (2008, 2023). Half of the sample was size-fractionated using nested sieves (200, 500, 1000, 2000, and 5000 µm), rinsed onto pre-weighed 0.2 mm Nitex mesh filters, and frozen at -20°C for dry biomass analysis. The dry weight biomass of each size fraction for each depth interval was determined by dividing the biomass by the seawater volume filtered through the net. For the May 17 day-night pair, the other half of the sample was also size-fractionated then preserved in sodium borate-buffered 4% formaldehyde. These preserved samples were imaged with a ZooSCAN version 3 at 2400 dpi, and uploaded to EcoTaxa (https://ecotaxa.obs-vlfr.fr/; Picheral et al., 2017) for manually validating as described in Maas et al. (2021). This dataset provides the abundance of zooplankton from each size fraction from each depth interval after accounting for fraction imaged and volume filtered. By dividing measured dry mass from the equivalent sample by this measured abundance, we calculated the average size of a zooplankton in that size fraction and net. We assumed the same average size organisms for the May 11 and 26 day-night pairs to calculate zooplankton abundance from these tows.

Table S1: Marine Snow Interaction Rate Estimates

Date	Upper Depth (m)	Lower Depth (m)	Marine Snow Abundance (# m^{-3})	Zooplankton Abundance (# m^{-3})	Interaction Rate (# m^{-3} d^{-1})	Normalized Interaction Rate
11-May	200	300	8260	308	400	-
	300	400	4970	57	44	-
	400	500	9860	53	82	-
17-May	200	300	57300	693	6240	15.6
	300	400	27900	164	718	16.2
	400	500	19400	54	165	2.0
26-May	200	300	117000	1530	28200	70.5
	300	400	74700	207	2430	54.7
	400	500	105000	135	2230	27.2

S11 - Quantifying the Fates of Marine Snow in the Mesopelagic Zone

An inverse model (Eq. 1) is used to assess the rates of transformation of large (marine snow; D > 0.5 mm) and smaller UVP-sampled particle abundances in the mesopelagic zone via linear regression. The UVP-determined particle volume distributions are converted to conserved volumes as detailed previously. Mean and vertical and temporal gradients of the daily mean small and marine snow-sized conserved volumes were calculated for six temporal intervals spanning different portions of the experiment and five 50 m vertical intervals from 225 to 425 m. Linear regression analysis is then applied to Eq. 1 to estimate the four or five parameters in the inverse model. This is repeated for each member of the ensemble and uncertainties are assessed as the standard deviation over the ensemble of retrievals.

The conserved volumes of marine-snow sized (V_L: D > 0.51 mm) and smaller (V_S: D < 0.51 mm) particles, as well as their gradients with respect to time and depth, were estimated via daily mean in situ particle imaging, for depths greater than 200 m (see *Supplementary Section S7*). The observed particle volumes were converted to conserved volumes assuming an ensemble of particle fractal dimension values to account for the uncertainties in particle porosity. The model coefficients were determined by linear regression and uncertainties in the model coefficients were determined using the standard deviation over the ensemble (Table 2). Two versions of the model are used: one where the marine snow sinking rate, w_L, is held constant over time and another where it is allowed to change as a linear function over the study's duration.

Additional References Used Only for the Supplementary Materials

D'Asaro, E.A., (2014). Turbulence in the upper-ocean mixed layer. *Annual Review of Marine Science*, **6**, 101-115, https://doi.org/10.1146/annurev-marine-010213-135138.

Estapa M.L., C.A. Durkin, W.H. Slade, C.L. Huffard, S.P. O'Neill, M.M. Omand , (2024) A new, global optical sediment trap calibration. *Limol. Oceanogr. Methods*: lom3.10592. https://doi.org/10.1002/lom3.10592.

Estapa M.L., Buesseler K., Durkin C.A., Omand M., Benitez-Nelson C.R., Roca-Martí M., et al. (2021). Biogenic sinking particle fluxes and sediment trap collection efficiency at Ocean Station Papa. *Elem. Sci. Anth.*, **9**, 00122. https://10.1525/elementa.2020.00122.

Giering, S.L.C, Cavan, E.L., Basedow, S.L., Briggs, N., Burd, A.B., Darroch, et al. (2020). Sinking organic particles in the ocean — Flux estimates from *in situ* optical devices. *Front. Mar. Sci.,* **6**:834, https://doi.org/10.3389/fmars.00834.

Honjo S., R. Francois, S. Manganini, J. Dymond, & R. Collier, (2000). Particle fluxes to the interior of the Southern Ocean in the Western Pacific sector along 170.3W. *Deep Sea Res. Part II*, **47**: 3521–3548, https://doi.org/10.1016/S0967-0645(00)00077-1.

Jackson, G.A., R. Maffione, D.K. Costello, A.L. Alldredge, B.E. Logan, H.G. Dam, (1997). Particle size spectra between 1 μm and 1 cm at Monterey Bay determined using multiple instruments. *Deep-Sea Res. I*, **44**:1739–1767, https://doi.org/10.1016/S0967-0637(97)00029-0.

Kilps, J.R., Logan, B.E. and Alldredge, A.L., (1994). Fractal dimensions of marine snow determined from image analysis of in situ photographs. *Deep Sea Res., Part I*, **41**, 1159-1169, https://doi.org/10.1016/0967-0637(94)90038-8.

Lam P.J., S.C. Doney, J.K.B. Bishop, (2011). The dynamic ocean biological pump: Insights from a global compilation of particulate organic carbon, $CaCO_3$, and opal concentration profiles from the mesopelagic. *Global Biogeochem. Cycles,* **25**, https://10.1029/2010GB003868.

Li, X., & B.E. Logan, (1995). Size distributions and fractal properties of particles during a simulated phytoplankton bloom in a mesocosm. *Deep-Sea Res., Part II*, 42:125–138, https://doi.org/10.1016/0967-0645(95)00008-E.

Logan, B.E., & D.B. Wilkinson, (1990). Fractal geometry of marine snow and other biological aggregates. *Limnol. Oceanogr*. **35**, 130–136. https://doi.org/10.2307/2837345.

Lombard, F., and others, (2019). Globally consistent quantitative observations of planktonic ecosystems. *Front. Mar. Sci.*, **6**, 1–21. https://doi.org/10.3389/fmars.2019.00196.

Lombardo, C.P., M.C. Gregg, (1989). Similarity scaling of viscous and thermal dissipation in a convecting surface boundary layer. *J. Geophys. Res.*, **94**(C5), 6273-6284, https://doi.org/10.1029/JC094iC05p06273.

Maas A.E., H. Gossner, M.J. Smith, L. Blanco-Bercial, (2021). Use of optical imaging datasets to assess biogeochemical contributions of the mesozooplankton. *J. Plankton Res.,* **43**, 475–491, https://doi.org/10.1093/plankt/fbab037.

McDonnell, A.M., Lam, P.J., Lamborg, C.H., Buesseler, K.O., Sanders, R., Riley, et al. (2015). The oceanographic toolbox for the collection of sinking and suspended marine particles. *Prog. Oceangr.*, **133**, 17-31, https://doi.org/10.1016/j.pocean.2015.01.007.

Mortlock R.A., P.N. Froelich, (1989). A simple method for the rapid determination of biogenic opal in pelagic marine sediments. *Deep Sea Res. A,* **36**(9): 1415–1426. https://doi.org/10.1016/0198-0149(89)90092-7.

Motoda, S., (1959). Devices of simple plankton apparatus. Memoirs of the Faculty of Fisheries Hokkaido University **7**: 73-94.

Picheral, M., S. Colin, J.O. Irisson. (2017). EcoTaxa, a tool for the taxonomic classification of images. https://ecotaxa.obs-vlfr.fr/.

Ploug, H., M.H. Iversen, G. Fischer G., (2008). Ballast, sinking velocity, and apparent diffusivity within marine snow and fecal pellets: Implications for substrate turnover by attached bacteria. *Limnol. Oceanogr.*, **53**:1878–1886, https://doi.org/10.4319/lo.2008.53.5.1878.

Risović, D., M. Martinis, (1996). Fractal dimension of suspended particles in seawater. *J. Colloid Interface Sci.*, **182**,199–203, https://doi.org/10.1006/jcis.1996.0451.

Schröder, S.M., Kiko, R. and Koch, R., (2020). MorphoCluster: Efficient annotation of plankton images by clustering. *Sensors*, **20**, 3060. https://doi.org/10.3390/s20113060.

Stamieszkin, K., Steinberg, D.K. and Maas, A.E., (2021). Fecal pellet production by mesozooplankton in the subarctic Northeast Pacific Ocean. *Limnol. Oceanogr.*, **66**(7), 2585-2597, https://doi.org/10.1002/lno.11774.

Vandromme, P. L. Stemmann, C. García-Comas, L. Berline, G. Gorsky, (2012). Assessing biases in computing size spectra of automatically classified zooplankton from imaging systems: A case study with the ZooScan integrated system. *Methods in Oceanogr.*. 1-2. 3-21. https://doi.org/10.1016/j.mio.2012.06.001.

Visser, A., 2001, Hydromechanical signals in the plankton. *Mar. Ecol. Prog. Ser.*, **222**, 1–24, https://doi.org/10.3354/meps222001**.**

Zhang, X. Y. Huot, D. Gray, H.M. Sosik, D. Siegel, L. Hu, et al., (2023). Particle size distribution at Ocean Station Papa from nanometers to millimeters constrained with intercomparison of seven methods. *Elem. Sci. Anth.*, **11**(1): 00094, https://doi.org/10.1525/elementa.2022.00094.

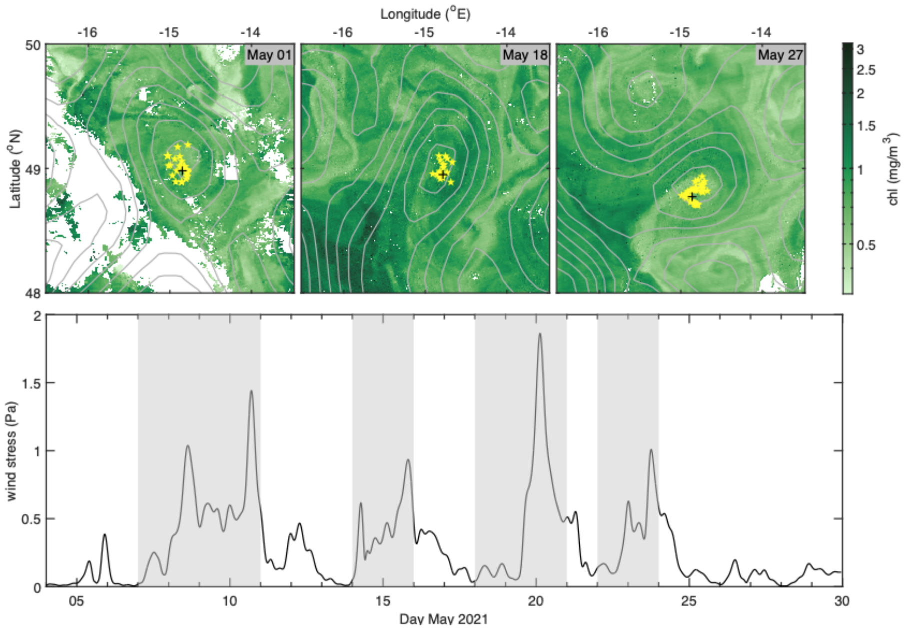

Figure S1: Upper panel: Satellite Chl and SSH of the eddy field for May 1, 18 and 27, 2021. Also shown is the track of Lagrangian float during the deployment. Lower panel: Wind stress time series showing in gray the days of ship work stoppages.

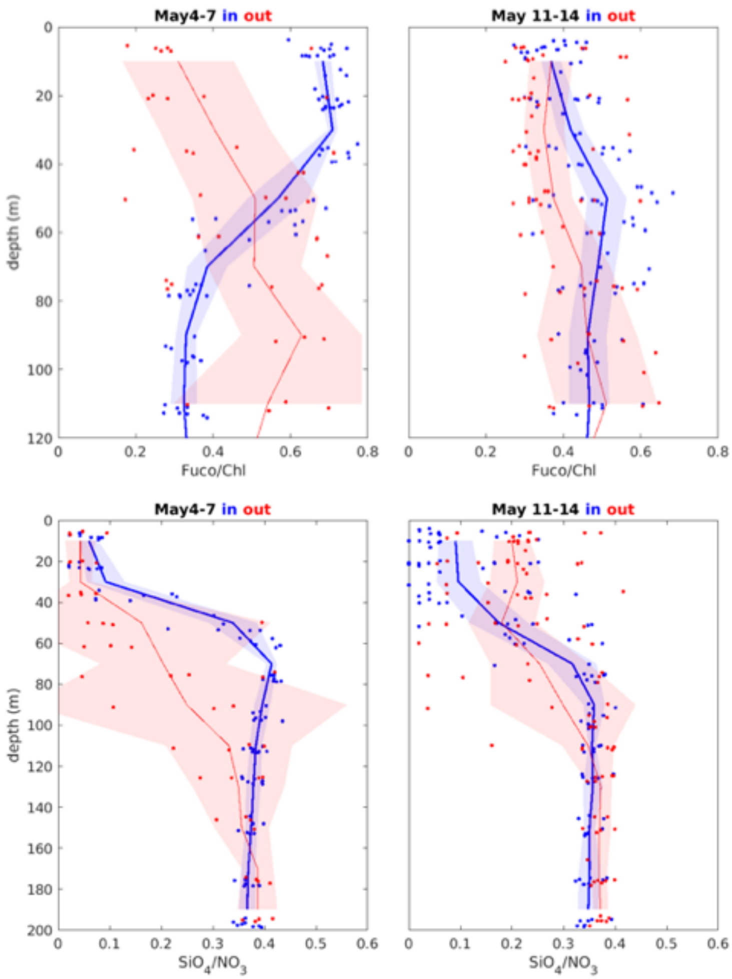

Figure S2 - Vertical profiles of ratios of the fucoxanthin (biomarker pigment for diatom abundances) to total chlorophyll a concentrations (Fuco/Chl) and the silicate to nitrate concentrations (SiO_4/NO_3) in the eddy (blue) and outside the eddy (red) both before (May 4-7) and after (May 11-14) the first large storm. In the eddy is defined as stations located within 15 km of the analyzed eddy center and outside of the eddy is defined as those stations that are 15 to 60 km from the eddy center.

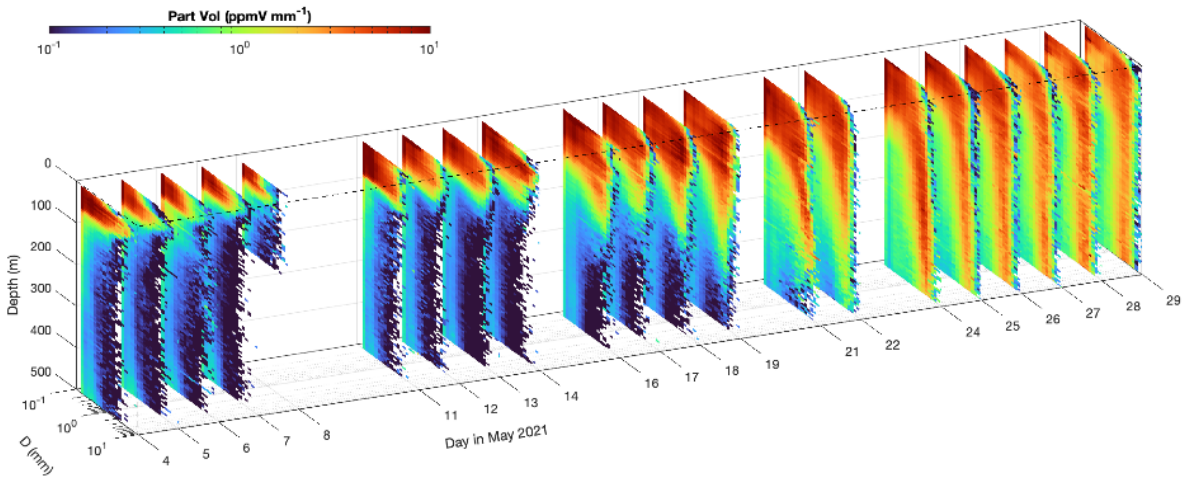

Figure S3: Daily mean profiles of the particle volume spectra (ppmV mm^{-1}) for all days during the EXPORTS NA study. Only data are shown that are within 15 km to the eddy center.

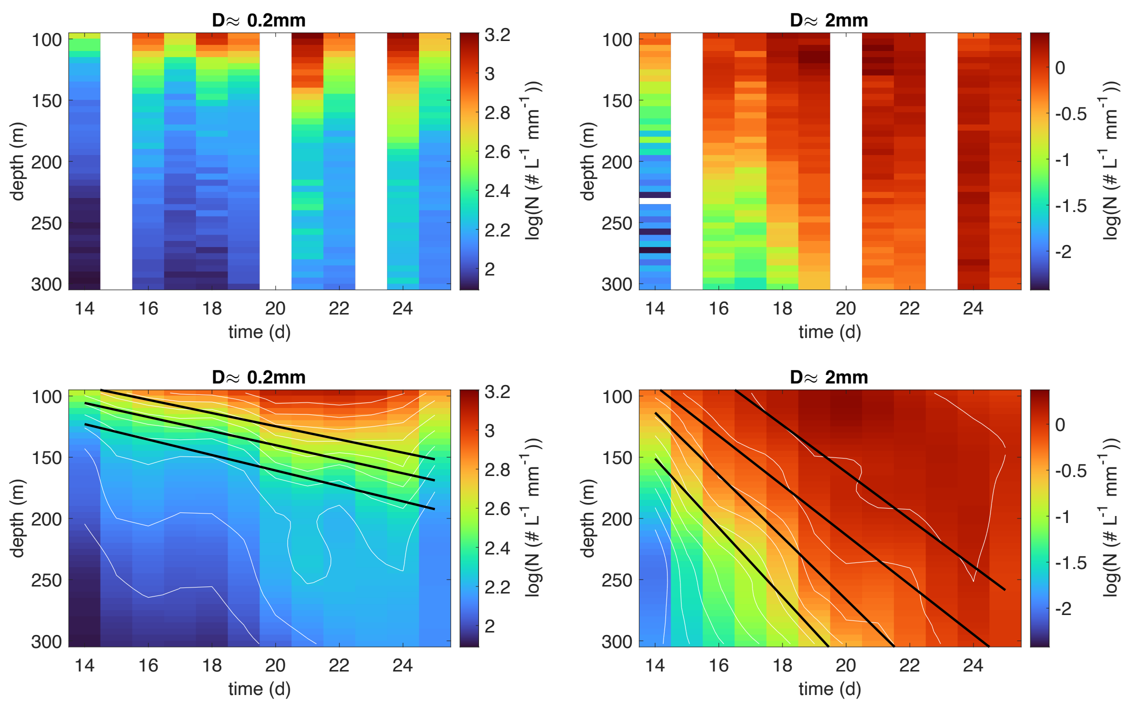

Figure S4: Example calculation of sinking speed fits. The upper panels are the daily mean profiles of 0.2 and 2 mm abundance in units of # L^{-1} mm^{-1} while the lower panels are the same after a LOESS fit surface is calculated. Six to ten lines following particle abundance isosurfaces are drawn and used to estimate sinking speed for each size bin. Mean and standard deviations over the ensemble of slope fits are reported in Fig. 2c. Shown here is a subset of the lines used.

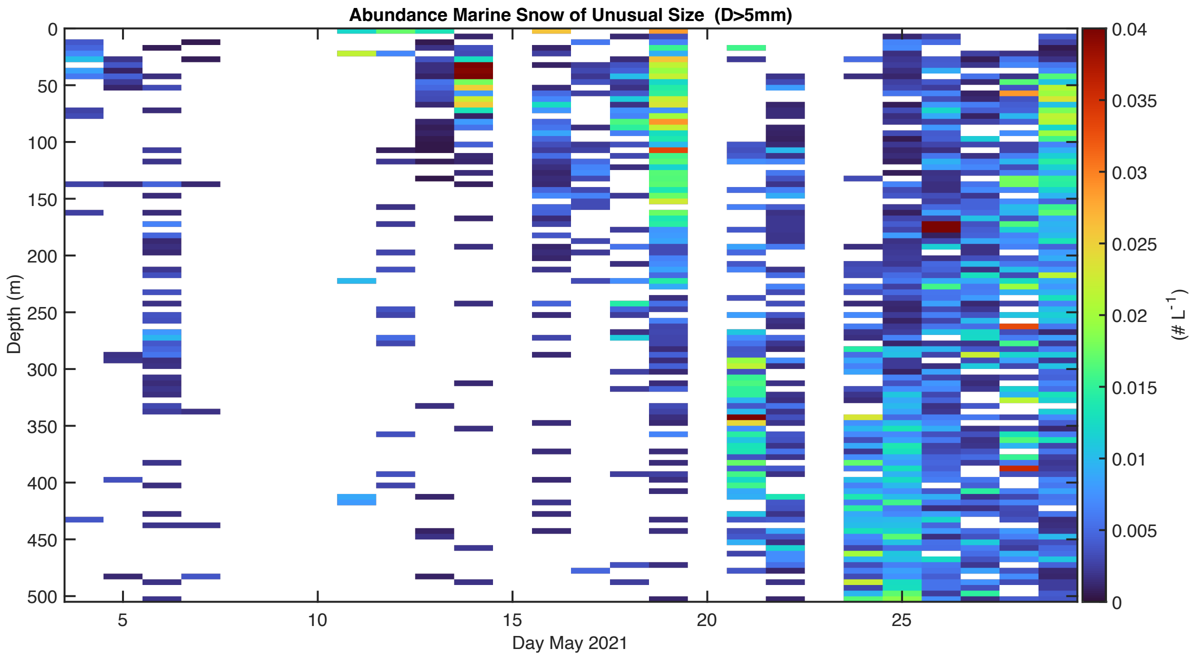

Figure S5: Abundance of marine snow particles with diameters > 5mm (marine snow particles of unusual size; MOUSs) calculated from UVP observations. Units are # L^{-1}.

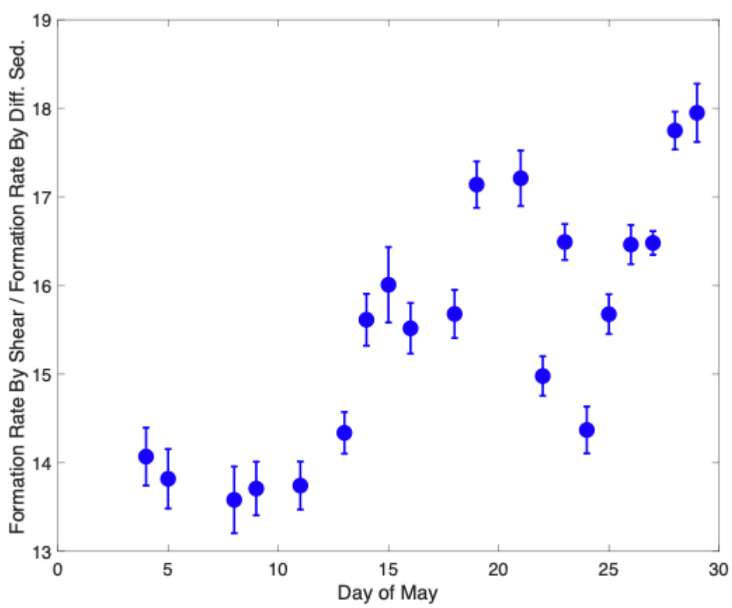

Figure S6: The ratio of the particle formation rates by turbulent shear to that by differential sedimentation for marine snow particles of unusual size (> 5 mm) in the 40–80 m depth-range.